C.E. SACLAY
DSM

SERVICE DE PHYSIQUE NUCLÉAIRE

DAPNIA-SPhN-96-06
INC-40007-104

01/1996

4π studies of the 1.8 - 4.8 GeV $^{3}He + {}^{nat}Ag, {}^{197}Au$ Reactions
I. Energy Deposition

K.B. Morley, K. Kwiatkowski, D.S. Bracken, E. Renshaw Foxford, V.E. Viola, L.W. Woo, N.R. Yoder, R. Legrain, E.C. Pollacco, C. Volant, R.G. Korteling, H. Breuer, J. Brzychczyk

DAPNIA

Le DAPNIA (**D**épartement d'**A**strophysique, de physique des Particles, de physique **N**ucléaire et de l'**I**nstrumentation **A**ssociée) regroupe les activités du Service d'Astrophysique (SAp), du Department de Physique des Particles Elémentaires (DPhPE) et du Department de Physique Nucléaire (DPhN).

Adresse : DAPNIA, Bâtiment 141
CEA Saclay
F -91191 Gif-sur-Yvette Cedex

To be published in Phys. Rev. C

INC-40007-104

EXCLUSIVE STUDIES OF THE 1.8 -4.8 GeV $^{3}He + ^{nat}Ag, ^{197}Au$ REACTIONS

1. ENERGY DEPOSITION

K. B. Morley, K. Kwiatkowski, D. S. Bracken, E. Renshaw Foxford, V. E. Viola,
L. W. Woo† and N. R. Yoder,
Departments of Chemistry and Physics and IUCF
Indiana University
Bloomington, IN 47405, USA

R. Legrain, E. C. Pollacco and C. Volant
CEA DAPNIA/SPhN, C.E. Saclay
91191 Gif-sur-Yvette Cedex, France

R. G. Korteling
Department of Chemistry
Simon Fraser University
Burnaby, BC, Canada

H. Breuer
Department of Physics
University of Maryland
College Park, MD 20742

and

J. Brzychczyk
Institute of Physics
Jagiellonian University
30-059 Krakow, Poland

Abstract

The 4π detector ISiS has been used to measure light-charged particles and intermediate-mass-fragments emitted in the 1.8 -4.8 GeV $^{3}He + ^{nat}Ag, ^{197}Au$ reactions. Ejectile multiplicity and total event kinetic energy distributions scale systematically with projectile energy and target mass, except for the ^{nat}Ag target at 3.6 and 4.8 GeV. For this system, a saturation in deposition energy is indicated by the data, suggesting the upper projectile energy for stopping has been reached. Maximum deposition energies of -950 MeV for the ^{nat}Ag target and -1600 MeV for the ^{197}Au target are inferred from the data. The results also demonstrate the importance of accounting for fast cascade processes in defining the excitation energy of the target-like residue. Correlations between various observable and the average IMF multiplicity indicate that the total thermal energy and total observed charge provide reliable gauges of the excitation energy of the fragmenting system. Comparison of the experimental distributions with intranuclear cascade predictions shows qualitative agreement.

---

†Sabbagh Associates, Bloomington, IN 47402, USA

1. Introduction

In order to investigate the behavior of nuclear matter under extreme conditions of temperature, target-projectile interactions that deposit excitation energies up to the total nuclear binding energy are required. For light-ion-induced reactions, this situation can be achieved via hard nucleon-nucleon scatterings and the excitation of Δ and higher resonances in central collisions, followed by rescattering and/or reabsorption of the decay pions in medium [1-4]. Nuclei excited in this way are unique in that a high energy-density region can be created in the nuclear interior on a time scale that is short ($\leq$ 30 fm/c [2,5]) with respect to the time for evolution of the nuclear mean field. Subsequent destabilization of the system occurs primarily by thermal processes--in contrast to heavy-ion-induced reactions, where compressional and rotational effects influence the breakup dynamics strongly. Thus, light-ion and heavy-ion studies complement one another in our attempts to understand the nuclear equation of state, each following distinctly different paths toward disassembly as they evolve in the nuclear temperature-density phase diagram.

A critical aspect of efforts to study the nuclear equation of state involves experimental determination of the thermal properties and subsequent decay modes of hot residues formed in energetic central collisions. For light-ion-induced reactions this is especially important due to the broad distribution of deposition energies and residue masses arising from fast cascade processes during the early stages of the collision [2-6]. Thus, it is essential to identify experimental observable that can be related to the energy deposition process. In turn, an understanding of the reaction dynamics is necessary to insure the reliability of deposition energy distributions predicted by transport models--which serve as vital input for theories designed to describe the decay dynamics of hot nuclear systems (see, for example, Ref. [4]).

In addition, geometric consequences of the reaction dynamics may influence the disintegration process in both light- and heavy-ion reactions. Such behavior has been indicated previously by intranuclear cascade calculations [7], and more recently by BUU calculations [8-10] that suggest unique donut- or bubble-shaped structures, or dispersed droplets, may exist temporarily during the time

evolution of the reaction [5,11-131.

Experimental attempts to test transport-model predictions for light-ion-induced reactions in the bombarding energy regime up to - 10 GeV/nucleon have focussed for the most part on hadron spectra. While such studies have demonstrated the relative success of the current codes, these comparisons relate most directly to the dissipation of energy by the projectile in the nuclear medium, rather than the question Of deposition energy in the hot residue. Definition of the latter quantity is less straightforward, especially for central collisions--demanding an understanding of energy evolution in the interaction zone and hadronization, dissipation time scales, and in-medium rescattering and reabsorption effects. The problem of pion reabsorption is a central issue, since this process plays an important role in the rapid conversion of relative projectile energy into internal excitation energy of the residue [2,4].

Early studies of energy deposition in energetic light-ion-induced reactions" demonstrated a significant probability for the formation of highly excited residual nuclei (14-16]. In addition, linear momentum transfer studies [17-19] showed that the deposition energy is a broad continuum. However, in order to evaluate the deposition energy more quantitatively, it is essential to perform exclusive studies of the residue breakup dynamics. Recently, Pienkowski et al. [20] have measured neutron multiplicities in 2.0 GeV proton- and ^{3}He-induced reactions on several targets. Their results are in approximate accord with intranuclear cascade predictions and indicate residue excitation energies up to $E^{*}/A \approx 5$ MeV/residue nucleon. Further, emulsion studies have suggested a saturation in the deposition energy at somewhat higher values of E^{*}/A [71.

In this paper, we present exclusive studies of charged-particle emission that examine energy deposition in the interaction of energetic ^{3}He projectiles with complex nuclei [21]. In Ref. [22] and the companion paper that follows [23], aspects of the data that relate to the multifragmentation process are investigated. In the following section, the experimental apparatus and data analysis procedures common to both papers are described.

ll. Experimental Measurement

The present study examines several experimental variables that directly reflect deposition energy in the target-rapidity source for 1.8, 3.6 and 4.8 GeV $^{3}He + ^{nat}Ag$, and 1.8 and 4.8 GeV + ^{197}Au reactions, as well as the correspondence between these results and intranuclear cascade code predictions. These results represent the first investigation of light-ion-induced reactions in which both light-charged particles (LCP = H and He) and intermediate-mass fragments (IMF: $3 < Z \leq 20$) are fully Z-identified with low energy thresholds and detected with large solid-angle coverage. The experiments were performed at the Saturne II accelerator at the Laboratoire National Saturne (E228) using the Indiana Silicon Sphere 4π detector array [ISiS].

A. The Indiana Silicon Sphere 4π Detector Array

The ISiS array, described in detail elsewhere [24], is based on a spherical geometry and is designed primarily for the study of light-ion-induced reactions. It consists of 162 triple detector telescopes--90 in the forward hemisphere and 72 in the backward hemisphere--covering the polar angular ranges from 14° to 86.5° and 93.5° to 166°. The design consists of eight rings, each composed of 18 truncated-pyramid telescope housings. To increase granularity at angles near 0°, the forwardmost ring is segmented into two components. A sketch of the detector configuration in the forward hemisphere is shown in Fig. 1.

Each telescope is composed of (1) a gas-ionization chamber (GIC) operated at 16-18 Torr of C_3F_8 gas; (2) a fully depleted 500 μm ion-implanted passivated silicon detector, Si(IP), and (3) a 28 mm thick CsI(Tℓ) crystal with light guide and photodiode readout. The CsI elements were also used as hit detectors that provided multiplicity information on minimum ionizing particles. Detectors are operated in a common gas volume; vacuum isolation is provided by a graphite-coated, 250 $\mu g/cm^2$ polypropylene window supported by an aluminum cage-like structure, matched to the geometry of the telescope housings and the passivated detector edges. The window also served as a cathode for the ion chambers. The telescope dynamic range permitted measurement of LCPs and IMFs Up to Z -20 with discrete charge resolution over the dynamic range $0.8 \leq E/A \leq 96$ MeV. The low energy threshold

includes the effects of target and window thicknesses, as well as the pressure in the gas-ionization chamber and the silicon surface dead layer. The Si(IP)/CsI(Tℓ) telescopes also provide particle identification (Z and A) for energetic H, He, Li and Be isotopes (E/A ≥ 8 MeV). The Si(IP) detectors constitute a critical component of the array, providing both excellent energy resolution and facilitating reliable energy calibrations for the GIC and CsI(Tℓ) elements.

Electronics for the ISiS array include custom-built preamplifier/shaper (PAS) units with fast and slow outputs for each detector element. Detector bias is computer-controlled via a custom-built system. Linear energy signals are digitized via Phillips 7164H peak-sensing CAMAC ADCs. Logic signals are processed via 16-channel CAMAC constant-fraction discriminators (LeCroy 3420) and Phillips 7186H CAMAC TDCs. More specific details of the electronics configuration and data-acquisition system are given in Ref. [24].

B. Experimental Details

Two types of targets were utilized in the experiments: 35 x 35 mm^2 foil targets mounted directly on 5 cm^2 target frames and 6 x 6 mm^2 foil targets supported at the sides by two 10 μm-diameter carbon fibers stretched vertically across the frame [25]. The experiments on ^{197}Au used a 6 x 6 mm^2 target of thickness 1.53 mg/cm^2. The experiments on ^{nat}Ag utilized both a 6 x 6 mm^2 target of thickness 1.08 mg/cm^2 and a 35 x 35 mm^2 foil of the same thickness. For most of the data acquisition, the smaller-area targets were used to ensure that detected events originated from interactions near the focus of the detector array. The larger-area targets were used to estimate the percentage of beam that missed the smaller targets, providing a basis for calculating absolute cross sections. A blank target was regularly placed in the target position to evaluate any contributions from beam halo striking the target frame. These were found to be negligible in all cases.

Beam intensities ranged from 0.5 - 1.1 x 10^8 particles/spill for these studies. The beam spill length was approximately 500 ms and the repetition cycle was 1.20, 2.56 and 4.01 sec at beam energies of 1.8, 3.6 and 4.8 GeV, respectively. The relative beam intensity was monitored throughout

the experiments by a secondary-emission monitor placed in front of the beam dump.

The experimental layout is illustrated in Fig. 2. Two x-y position-sensitive beam profilers, one upstream and one downstream of ISiS, provided information for beam tuning. The secondary emission monitor was located just downstream of the second profiler. A 50 cm-long lead collimator (inner diameter = 9 cm, outer diameter = 18 cm), located 1.3 meters upstream of the target, was inserted to protect those silicon detectors nearest the beam axis from radiation damage during beam tuning. In addition, an active-collimator system consisting of eight fast-plastic scintillator segments was located directly downstream of the lead collimator at the entrance to ISiS. The active-collimator system was divided into an inner and outer collimator. The inner active collimator was located inside the beam pipe and consisted of four, 2 cm-thick paddles shaped to form four quadrants of a disk with an inner diameter of 3 cm and an outer diameter of 16 cm. The four outer active collimators were arranged to surround the outside of the beam pipe and consisted of $50 \times 20\ cm^2$ paddles of thickness approximately 0.6 cm. This combined system shadowed the entire active cross sectional area of ISiS relative to the beam axis.

A recoil array attached to the downstream end of ISiS was designed to detect heavy recoil nuclei and a fast-plastic wall (ARCOLE) was located 5 m downstream to detect fast leading particles. Results from these components of the experiment will be discussed in subsequent publications.

For the data presented here, a multiplicity of two in the silicon fast logic was set as a minimum-bias trigger. The signal conditioning, trigger logic, and data acquisition for ISiS are described in more detail in Ref. 24. Data were written directly to disk and then copied to 4 mm and 8 mm tapes. Scalers were read and written to disk at the beginning and end of every beam spill. Detector voltage and leakage currents were also written at preset intervals. The coincidence information from the active collimators was written for every ISiS event. In addition, ADC hit registers for all CsI(Tℓ) detectors were checked whenever an ISiS event occurred. If a CsI(Tℓ) detector registered an event above a fixed threshold energy, but without its corresponding silicon detector, then the CsI(Tℓ) ADC channel was read and included in the event buffer. These signals are referred to as minimum-ionizing-particle (MIP)

signals and correspond to energetic particles (primarily hydrogen isotopes) with energy fess too low produce a trigger signal from the silicon detectors that exceeded the fast-timing threshold. The acquisition-system dead-time was maintained between 20% and 35% (during beam spills) through most of the experiments.

Spectra from selected ISiS telescopes were set up to monitor left-right and up-down beam asymmetries. In addition, a "spill-clock spectrum" and spill-intensity spectra were implemented to monitor the number of ISiS events as a function of time relative to the beginning of the beam spill. Individual energy spectra for ail detectors were monitored throughout the run, both single and two-dimensional, as were time spectra from the silicon time-to-digital converters.

The silicon detectors were calibrated through the test inputs of the preamplifier/shaping-amplifier units with CAMAC computer controlled (C3P) pulsers [26]. One channel in each silicon P unit was cross-calibrated using a charge-terminated ORTEC 448 precision pulse generator (calibra with a ^{241}Am source) tied to the detector input of the PAS module. ionization-chamber calibrations were also made with a ^{241}Am alpha source, with and without C_3F_8 gas in the ISiS detector array. Energy-loss corrections (based on window thickness measurements obtained later by weighing the polypropylene windows) were applied to the calibration data.

C. Data Analysis

Energy calibrations for the silicon detectors were determined by extracting the computer-controlled pulser centroids in the silicon energy spectra and fitting a linear equation to the results. Absolute calibrations were extracted relative to the ^{241}Am calibration of the ORTEC precision pulse generator. The calibrations were found consistent to about 1.5% with ^{241}Am alpha-source data and light-charged particle punch-through energies. The ionization chambers were calibrated using a computer program based on helium-ion energy-loss data for C_3F_8 [27] and corresponding points of different He energy in the calibrated silicon detector. The absolute errors in the ionization-chamber calibrations are about ± 5%.

The CsI(Tℓ) crystals were calibrated in a similar manner to the ionization-chambers. Each calibrated-silicon energy signal was plotted versus its corresponding uncalibrated photodiode signal. Because the light output from a CsI(Tℓ) crystal varies as a function of the particle type, each identified line (i.e. p, d, t, He, and Li) was calibrated separately. An energy loss program [28] was used to obtain the CsI energy from the known energy loss in the silicon detector and a linear equation was fit to the CsI(Tℓ) energy versus channel number. Because the calibrations for all isotopes of a given element were similar, the calibration values for a given telescope and charge were averaged together to facilitate the data replay.

Once the energy calibration values were determined, a set of computer gates was established in each ring of ionization-chamber/silicon pairs. When overlaid, the 18 individual spectra from a given ring (fixed angular range) showed excellent consistency in both charge identification and energy characteristics [24]. Individual light-charged particle (p, d, t, ^{3}He, ^{4}He and Li) gates were set for each silicon/photodiode pair. The energies of IMFs identified in the ionization-chamber/silicon gates were corrected for energy loss in the target (assuming the interaction was at one-half the target thickness), polypropylene window and silicon detector dead-layer. For LCPs, these corrections are very small and were therefore not applied.

The reduced event-by-event data were rewritten to tape with the additional information of fragment charge, telescope identification, calibrated energies in each detector element, and total calibrated energy, including corrections for energy-loss due to target and GIC-window thicknesses. In subsequent replay of the repacked data, additional gates on the energy and timing signals from the active collimators and timing signals from the silicon detectors were included to select valid signals. Events which fired in coincidence with high energy light-charged particles in the active collimators (about 100/~ of the events) were eliminated from the analysis in replay. A gate was also set to eliminate data corresponding to the first 40-70 ms of the beam spill.

The number of valid trigger events (multiplicity $\geq$ 2) for each system and the number of valid trigger events in which at least one IMF was detected are tabulated in Table 1.

III. Experimental Results

The distribution of excitation energies deposited in the residual nuclei during the initial cascade in these reactions has been examined via several experimental variables believed to be strongly correlated with deposition energy. These include: observed multiplicity distributions for LCP's (N_{LCP}), IMF's (N_{IMF}) and total charged particles (N_{tot}); total observed charge (Z_{obs}), and total observed transverse and thermal energy ($E_{\perp}$ and E_{th}, defined later). Results are presented in terms of relative probability distributions, with $\sum N/N = 1$. Self-consistent comparison among the five data sets was assured by removing from the analysis any telescope that was not continuously functional throughout the experiment. This resulted in an identical detector acceptance of 67% of 4π obtained in the ^{3}He + ^{nat}Ag reaction and 69% for the ^{3}He + ^{197}Au reaction.

A. Distributions

One important gauge of deposition energy is the number of IMFs emitted in a given event. IMF multiplicity is predicted to be strongly correlated with excitation energy [29-31], at least until the internal energy of the system approaches the vaporization limit. In Fig. 3, the observed IMF multiplicity distributions for the 1.8 -4.8 GeV ^{3}He + ^{nat}Ag, ^{197}Au systems are shown. As a general trend, the maximum observed IMF multiplicity scales with projectile energy. However, the IMF multiplicity distributions for the 3,6 and 4.8 GeV ^{3}He + ^{nat}Ag reactions are nearly identical, suggesting that deposition energy is similar for these two projectile energies.

Comparison of the results for the two targets at 4.8 GeV bombarding energy shows a distinctly higher multiplicity for ^{197}Au (M_{IMF}^{max} - 10) relative to ^{nat}Ag (M_{IMF}^{max} - 7) at the 10^{-6} relative probability level. This is roughly in proportion to the upper limits of excitation energy predicted for these two systems by intranuclear cascade calculations [3]: (- 1500 MeV for ^{197}Au and -1000 MeV for ^{nat}Ag). However, the larger mass of the ^{197}Au target may also influence this result. Finally, the 1.8 'eV ^{3}He + ^{nat}Ag system, which is predicted to have the lowest average excitation energy, exhibits the lowest average multiplicity, although the ^{197}Au system at 1.8 GeV is not significantly higher, due in part to the

proximity of this system to the multifragmentation threshold (29-31]. We note here that the IMF multiplicity distribution measured in this work for 4.8 GeV $^{3}He + ^{197}Au$ differ distinctly from that reported in Ref. 32 for the similar 4.0 GeV $^{4}He + ^{197}Au$ system. This is discussed in more detail in Ref. 23.

The IMF multiplicities provide a rather coarse gauge of the excitation energy distributions due to the relatively small number of fragments. As an alternative, we examine two observable commonly used in heavy-km reaction studies [16,33,34], the multiplicities of light-charged particles (N_{LCP}) and total charged particles ($N_{tot} = N_{LCP} + N_{IMF}$). These are shown in Fig. 4 and, for the most part, are similar in character to those for IMFs. One distinct difference between the LCP/total charged particle distributions and those for IMFs is found in the 3.6 and 4.8 GeV $^{3}He + ^{nat}Ag$ systems, where the higher projectile energy leads to higher multiplicities. However, the LCP distribution includes a significant contribution from ejectiles emitted during the fast cascade/non-equilibrium stages of the reaction. These latter contributions are illustrated in Fig. 5, which shows relative differential cross sections for the fragment kinetic energy distributions gated on M_{IMF} = 2 for He, Li and C fragments emitted at 14° - 22° in the 4.8 GeV $^{3}He + ^{197}Au$ reaction. The significant yields of energetic ejectiles are apparent and demonstrate that even for the more violent events, non-equilibrium processes compose an important fraction of the yield. These observations suggest that the LCP distributions of Fig. 4 may serve as a better gauge of the energy dissipated by the projectile than the actual deposition energy in the hot residual nucleus. Also shown in Fig. 5 are two-~ mponent moving-source fits [35] to the Li and C data (solid lines). The dashed lines give the equilibrium-like fit component and the difference represents nonequilibrium processes.

To investigate the effect of nonequilibrium emission, we have schematically separated all ejectile Spectra into thermal and fast components. The division takes advantage of the excellent energy definition provided by the silicon elements in the ISiS array, combined with minimal source kinematic effects in these reactions [23] --which provide nearly complete, high quality spectra for all fragments over the full angular range. The separation procedure is based on analysis of the systematic behavior of the Maxwellian-like spectra and the distinct slope change in the exponential tails of the LCP and IMF

inclusive spectra (especially prominent for Z = 2 fragments in Fig. 5). For each Z value, thermal charged particles (N_{th}) are defined to be those ejectiles with energies (&) below a cutoff energy, $\varepsilon_{th}^{max} = C_o \cdot Z + \varepsilon_o$. Here Z_f is the fragment charge; C_o is Z-dependent peak parameter determined from fits to the most probable peak energies, and ε_o = 31 MeV is a constant based upon the two-component moving-source fits illustrated in Fig. 5. The parameter C_o is weakly dependent on both target mass and beam energy. Values of ε^i are evaluated in the source reference frame, as determined from both rapidity and moving-source fits to the spectra [23,35]. Fragments with energies above this ε^{max} Cutoff energy are labelled fast (N_{fast}), and are important primarily for Z = 1-4 ejectiles. The extracted observable show little sensitivity to the division point over a ±1 O MeV interval in ε_o.

The results of this analysis are shown in Fig. 6, where distributions for N_{th} and N_{fast} are plotted. For the Ag target, it is observed that the multiplicity distributions for thermal events are nearly the same at 3.6 GeV and 4.8 GeV. However, the fast particles are clearly enhanced at the higher bombarding energy, suggesting less stopping and a more intense spray of fast ejectiles. This analysis emphasizes the need to eliminate fast cascade/nonequilibrium events whenever particle multiplicity or fragment charge/isotope distributions are used as an indicator of excitation energy.

Another observable that provides a continuous distribution is the total energy of all fragments emitted in an event, E_{tot}, which, in principle, should be related to the excitation energy of the emitting source. In Fig. 7, we show the distributions for the systems studied here. At the 10^{-5} probability level, event energies are observed up to E_{tot} -900 MeV for Ag and E_{tot} -1200 MeV for ^{197}Au at the highest bombarding energy. However, as is evident from the spectra in Fig. 5, a Significant fraction of E_{tot} may originate in fast cascade/nonequilibrium events that are not representative of the excitation energy of the fragmenting source.

In order to define an observable that is more directly related to the excitation energy of the multifragmenting system, provides a continuous distribution, and minimizes preequilibrium contributions, we have constructed a sum of the kinetic energies for all thermal ejectiles in an event. This quantity is defined as the total thermalized energy, $E_{th} = \Sigma\varepsilon_{th}^i$. This definition does not necessarily imply full

statistical equilibrium, but rather is an indicator of the internal energy available to drive the disassembly process.

The E_{th} distributions shown in Fig. 8 scale systematically with projectile energy and target mass, analogous to the behavior of the IMF and thermal ejectile multiplicity distributions. The 3.6 and 4.8 GeV E_{th} distributions are also nearly identical for the ^{3}He + Ag system. The similarity of the IMF, N_{th}, and E_{th} distributions suggests that the deposition energy saturates near 4 GeV. Similar saturation effects have previously been proposed from interpretation of 3-5 GeV proton interactions with emulsions [6]. Many effects contribute to the saturation of deposition energy in this energy range, including: the leveling of the total N-N cross section; increasingly forward-peaked N-N elastic and inelastic angular distributions; the increase in the secondary pion momenta above the (3,3) resonance, and, as pointed out in Refs. 6 and 13, the depletion of the nucleon density in the central collision region. The net result is a saturation and/or decrease in the transverse N-N momentum transfer [36], which produces an increasingly forward-focussed flow of energy with increasing projectile energy beyond a few GeV.

Also shown in Fig. 8 is the correlation between E_{th} and the total observed transverse energy per event, $E_\perp = \sum \sin^2 \theta \, E_i$. The error bars represent the full-width at half maximum of the distributions. In calculating $E_\perp$, no distinction is made between thermal and fast ejectiles, consistent with the use of this variable in heavy-ion studies. It is observed that there is good scaling between E_{th} and $E_\perp$ at the highest thermal energies. However, it should be noted that his agreement is in part due to the cumulative sum of small nonequilibrium components in the calculation of $E_\perp$, which exert a non-negligible influence on its magnitude. As E_{th} decreases, $E_\perp$ systematically deviates above E_{th}, presumably due to the more peripheral origin of these events, accompanied by increased probability for nonequilibrium emission. For the ^{3}He + ^{nat}Ag system, $E_\perp$ is systematically ~ 10% higher at 4.8 GeV than at 3.6 GeV, consistent with the results of Fig. 7. This suggests that $E_\perp$ serves as a better gauge of the energy dissipated by the projectile, whereas E_{th} relates more directly to the energy deposited in the heavy residual nucleus.

At the 10^{-6} probability level, the maximum observed values of E_{th} ~ 350 MeV for the ^{nat}Ag

residue and ~ 550 MeV for ^{197}Au indicate the attainment of significant deposition energies in these reactions. These values translate into maximum deposition energies of the order of 950 MeV for the ^{nat}Ag residue and 1600 MeV for the ^{197}Au residue, when first-order corrections are applied for solid angle losses, neutron emission [20] and separation energies (based on charge distributions corresponding to these events). Allowing for mass loss during the fast cascade, as predicted by INC calculations [3], these deposition energies correspond to maxima of ~12 MeV/nucleon and ~10 MeV/nucleon for the Ag and Au residues, respectively. Thus, the E_{th} distributions indicate that we are observing events in which deposition energies in excess of the total nuclear binding energy are achieved. However, the widths of the excitation energy distributions for a given observable (see Sec. III. B.) are quite broad and thus influence our estimates of the maximum deposition energies.

Another observable that provides a useful gauge of the collision violence is the total detected charge, Z_{obs}. Since the ISiS array does not measure low energy recoil nuclei, Z_{obs} is directly related to the sum Of target plus projectile protons that participate in the reaction and subsequently appear as LCPs and IMFs. Therefore, Z_{obs} should be strongly correlated with deposition energy. The Z_{obs} distributions are shown in Fig. 9, and correspond well with the behavior of the observable discussed above. For the Ag system, the 3.6 and 4.8 GeV $^{3}He + ^{nat}Ag$ results for Z_{obs} are nearly identical, further substantiating the conclusion that deposition energy saturates near a bombarding energy Of 4 GeV for the $^{3}He + ^{nat}Ag$ system. Otherwise, the Z_{tot} distributions scale systematically with bombarding energy and target mass. For each target, the distributions in observed charge decrease monotonically up to a value consistent with the total charge available in the reaction, corrected for detector geometric acceptance to first order ($Z \sim 33$ for Ag and $Z \sim 56$ for Au). Thereafter, the distributions decrease more rapidly, although some events are detected that contain Up to 90% of the total charge. Thus, both the Z_{obs} and E_{th} distributions at the 4.8 GeV bombarding energy demonstrate that we are observing events in which large deposition energies lead to highly disrupted final states.

B. Gauges of Excitation Energy

All models of multifragmentation [29-31 ,37] predict that the IMF multiplicity is strongly correlated with excitation energy, at least Up to very high excitation energies, beyond which the average IMF multiplicity begins to decrease with a corresponding increase in LCP multiplicities. The decrease at higher energy is confirmed by experimental data from heavy-ion-induced reactions [38,39]. The high excitation energies that lead to a decline in average IMF multiplicity, if accessible in light-ion-induced reactions, should be found in correlations with other observables. Under this assumption, the average IMF multiplicity, $\langle N_{IMF} \rangle$, has been plotted against light-charged-particle multiplicity (N_{LCP}), total charged-particle multiplicity (N_{tot}), total observed charge (Z_{obs}) and total thermal energy (E_{th}), as shown in Figs. 10 and ıl. It is found that for low N_{LCP} (the most peripheral collisions), the average observed IMF multiplicity increases monotonically. As N_{LCP} increases, the average number of IMFs emitted from the 4.8 GeV $^{3}He + ^{197}Au$ systems increases above those of the other systems. For all the systems, $\langle N_{IMF} \rangle$ becomes nearly constant for large values of N_{LCP}, reaching maxima near $\langle N_{IMF} \rangle$ 0.4 for the 1.8 GeV $^{3}He + ^{nat}Ag, ^{197}Au$ systems, $\langle N_{IMF} \rangle$ -0.75 for the 3.6 and 4.8 GeV $^{3}He + ^{nat}Ag$ systems, and $\langle N_{IMF} \rangle$ -1.5 for the 4.8 GeV $^{3}He + ^{197}Au$ system. These results are consistent with INC calculations, which predict only a weak positive correlation between the fast LCP multiplicity and large deposition energies due to the very large fluctuations associated with the cascade [2,3]. Fluctuations in the residue disassembly process provide a further complication, as illustrated in Fig. 12, where we show the LCP distributions as a function of IMF multiplicity for the $^{3}He + ^{197}Au$ reaction at 4.8 GeV. Thus, the LCP multiplicity in central collisions appears to be a poor gauge of the deposition energy. This result contrasts with the conclusions of Ref. 16, where particle identification thresholds were an order Of magnitude higher.

A more sensitive correlation is obtained when total charged-particle multiplicities are compared with $\langle N_{IMF} \rangle$; however, this may be in large part due to autocorrelation effects. All systems yield similar results for peripheral reactions, with the 4.8 GeV $^{3}He + ^{nat}Au$ system extending beyond the others at high values of N_{tot}. For the most dissipative collisions, the maximum $\langle N_{IMF} \rangle$ reaches values approximately twice as large as for LCPs alone (i.e. maxima of -1.2 for the 1.8 GeV systems, -1.5 for

the 3.6 and 4.8 GeV $^{3}He + ^{nat}Ag$ systems, and -3.0 for the 4.8 GeV $^{3}He + ^{197}Au$ system). These results are very similar to data from comparable systems in heavy-ion-induced reactions [40-42], although heavy ions tend to yield somewhat larger maximum values of $<N_{IMF}>$ and N_{tot} than are observed here.

The most sensitive correlations with IMF multiplicities are found for total detected charge, Z_{obs}, and the total thermalized energy, E_{th}. For Z_{obs}, we find that with the exception of 1.8 GeV $^{3}He + ^{197}Au$ the systems have nearly identical behavior over the entire observed range in Z_{obs}, with a slope of approximately 12 charge units/IMF emitted, on average (Fig. 11). However, there is a large degree of auto-correlation between $<N_{IMF}>$ and Z_{obs}, since higher IMF multiplicities tend to result in a higher total IMF charge and therefore higher Z_{obs}. The deviation observed in the 1.8 GeV $^{3}He + ^{197}Au$ system is most likely due to contributions from fission, which are most significant for this system.

The correlations for thermalized energy are very similar to those of Z_{obs}. Total energy and total transverse energy were also investigated. However, these yielded weaker correlations than E_{th}, most likely due to the inclusion of a larger number of nonequilibrium particles (primarily H and He isotopes) in the calculations of the total energy and total transverse energy. Because nonequilibrium particles are emitted in the early-to-intermediate stages of the reaction, they are less valid indicators of the residue excitation energy.

One point that should be made is that E_{th}, total energy and total transverse energy all include contributions from the Coulomb repulsion energy of the emitted fragments and the thermal energy of the source, as well as any possible collective expansion of the system. The last of these may arise from either decompression of the system, or from thermal expansion. Compressional effects are expected to be small in light-ion-induced reactions, since the projectile-target interaction results in little density compression [15]. Decompression should be distinguished from thermal expansion effects, which may be present in light-ion-induced reactions (e.g., expansion following multiple pion absorption in a localized central region of the nucleus). The Coulomb energy at near normal nuclear density is not very sensitive to the excitation energy of the system. It is simply a measure of the repulsion of the

fragments from the effective source; i.e. the geometry of the system at breakup.

Based on these correlations, for light-ion-induced reactions the total observed charge and thermalized energy appear to provide reliable measures of the energy dissipated by the projectile into the internal energy of the system. However, it should be stressed that in all cases, the width of the distributions is quite broad, as illustrated by Fig. 12. Thus, the use of average quantities must be interpreted with some caution.

IV. Intranuclear Cascade Simulations

In order to make meaningful comparisons between multifragmentation models and the data, it is necessary to account for the underlying collision dynamics. To achieve this, models that treat the disassembly of excited residues must be joined to some appropriate transport model to predict the mass and excitation energy distributions of the excited residues, as well as other quantities related to the dissipation process such as fast proton distributions.

The complexity associated with reactions at intermediate energies is well illustrated by the results of linear momentum transfer and mass-yield measurements carried out during the past decade [17-19,43]. These studies have demonstrated that the initial target-projectile interaction generates a broad distribution of residual nuclei and excitation energies. For an understanding of multifragmentation, it is therefore essential to obtain these distributions through a realistic treatment of the impact geometry, excitation mechanisms, and preequilibrium emission. In the case of light-ion-induced reactions, it is especially important to account for the initial energy dissipation stage since there are a relatively small number of hard N-N collisions, and there is a substantial transparency for incoming particles. For light-ion-induced reactions well above the Fermi energy, where there is little time for evolution of the mean field, intranuclear cascade models [2,3,7] can be used to evaluate these features, which are related to the initial energy dissipation. For heavy-ions, however, the evolution of the mean field of the colliding nuclear system is also significantly influenced by the reaction dynamics, and BUU approaches are required [8-10,44-46].

In this section, energy deposition in the $^{3}He + ^{nat}Ag, ^{197}Au$ reactions is investigated using the Weizmann Institute version of the intranuclear cascade code ISABEL [3]. The intranuclear cascade (INC) results reported here were performed using the fast rearrangement options and sequential-collision exclusion within a 1.1 fm distance. These options emphasize the formation of highly excited residual nuclei--a condition necessary to enhance the probability for multifragmentation [4]. The cascade-cascade interaction serves to increase pion absorption by allowing particles that have already undergone collisions to interact further. In calculations with fast rearrangement, the volume in which an interaction takes place is instantly filled (overall density is lowered) so that additional collisions can occur in the region. This assumption has been shown to reproduce experimental data for central collisions in heavy-ion-induced reactions at similar projectile E/A values, and at the same time account for fast nucleon spectra and multiplicities [3].

ISABEL calculations were carried out for the $^{3}He + ^{107}Ag, ^{197}Au$ systems for bombarding energies between 0.27 and 5.8 GeV. The calculation for each interaction was halted when the energy of the nucleons from each cascade fell below the energy needed to escape the nuclear well. At this point, the mass, charge, momentum vector, and excitation energy of the residual nucleus were calculated. The subsequent decay of these excited residues can then be treated in a separate calculation [4].

In Fig. 13, the **average excitation energy** of the residual nuclei predicted by the ISABEL code for the $^{3}He + ^{nat}Ag, ^{197}Au$ systems is shown for incident energies below 6 GeV. The curves 'how 'he average excitation energy for three impact parameter regimes: central collisions (b c 2.6 fro), intermediate impact parameters ($2.6 \leq b \leq 4.4$ fro), and peripheral interactions ($b \geq 4.4$ fro). Assuming a radius parameter of $r_0 \cong 1.4$ fm, these values correspond to approximately 10%, 20% and 70% of the total reaction cross section, respectively. It is observed that for events with the largest impact parameters, i.e. most of the cross section, the average excitation energy, $\langle E^{*} \rangle$, remains relatively low and insensitive to bombarding energy, E_{beam}. With decreasing impact parameter, however, the average excitation **energy increases much** more **rapidly with** bombarding energy. For the $^{3}He + ^{nat}Ag$

system, the code predicts a saturation in average excitation above about 4 GeV for central collisions. This is due to (1) increasing transparency and (2) greater pre-equilibrium emission that accompanies the higher bombarding energies, both of which are reflections of the saturation in the N-N reaction cross-sections. At higher energies, the N-N cross sections become more forward focused and there is an increase in the energy of the secondary pions, decreasing the likelihood of A excitations. Also, because of the large mass fess during the initial cascade (Fig. 14), the effective density of nucleons is noticeably reduced in the later stages of the cascade.

Fig. 15 shows the excitation energy distributions predicted by ISABEL for the 1.8 and 4.8 GeV $^{3}He + ^{197}Au$ and 1.8, 3.6 and 4.8 GeV $^{3}He + ^{107}Ag$ systems for collisions which deposit excitation energies greater than $E^{*} \geq 50$ MeV. As expected, the distributions extend to higher excitation energies for the 4.8 GeV projectiles than for the 1.8 GeV. When comparing the 1.8 and 4.8 GeV results, the excitation energy distribution for ^{197}Au extends to significantly higher residue energies than for the ^{107}Ag target. One simple explanation for this is the difference in size Of the two systems. The average thickness, $\langle t \rangle$, of a nucleus is given by $\langle t \rangle \sim 1.3 r_0 A^{1/3}$; $\langle t \rangle \sim 9.3$ fm for ^{197}Au and $\langle t \rangle \sim 7.6$ for ^{107}Ag. For a total N-N cross section of 40 mb, the average thickness for ^{197}Au is about 4.4 times greater than the nucleon mean free path, as compared to 3.7 for ^{nat}Ag.

The qualitative correspondence between the data in Figs. 6-8 and the ISABEL calculations is good. Most significant, the INC calculations for the $^{3}He + ^{nat}Ag$ system also indicate that approximate saturation in the residue deposition energy is reached at a bombarding energy near 4 GeV. This is apparent both in the excitation function of Fig. 13 and in the nearly identical probability distributions for the 3.6 and 4.8 GeV cases in Fig. 15. The INC 'excitation energy distributions have also been compared with predictions based on BUU calculations [15]. The trends--especially the approach to excitation energy saturation near 4 GeV--track quite well. It should also be noted that both BUU and INC calculations indicate that the post-cascade residue exists in a state of depleted density (i.e. $\rho < \rho_0$), perhaps involving bubble-like structures in the nuclear interior [5,7]. Hence, the reaction dynamics may play an important role in the breakup geometry of the post-cascade residues. Ideally, this depletion

effect should be incorporated in the initial stages of theoretical treatments of the decay dynamics.

More generally, the following systematic features of the data are reflected by the INC calculations. For both systems, the excitation energy distributions extend to distinctly higher energies when the projectile energy increases from 1.8 to 4.8 GeV. The distributions also scale approximately with target mass for a given bombarding energy. Another correspondence is that the code predicts the excitation energy distribution for the 1.8 GeV ^{3}He + ^{197}Au system to be just slightly below that for 3.6 GeV ^{3}He + ^{nat}Ag; the multiplicity distributions for these two systems exhibit similar behavior. As a gauge for comparison with the INC calculations, the total thermalized energy appears to be a particularly useful parameter in that it is a continuous variable, includes minimal pre-equilibrium contributions, and in principle, can be directly related to the residue excitation energy. However, the direct connection between the excitation energy predictions of transport models and experimental observables is non-trivial and in this paper we only attempt to investigate the qualitative relationship.

Analysis of the INC results also sheds light on two other aspects of the data. First, the larger charged particle multiplicities for the ^{3}He + ^{nat}Ag system at 4.8 GeV relative to 3.6 GeV (Figs. 4 and 6), were ascribed to fast particle emission. The INC calculations support this interpretation, predicting more fast cascade particles at 4.8 GeV than at 3.6 GeV, despite nearly identical excitation energy distributions. Second, the maximum excitation energies predicted by the INC code at 4.8 GeV are of the order of 1.0 GeV for the ^{nat}Ag target and 1.5 GeV for ^{197}Au. These values roughly correspond to those inferred from the maximum experimentally observed E_{th} results in Fig. 8. Although the fraction of events with $E^{*} \geq 500$ MeV is much higher for the ^{197}Au target (Fig. 15), the excitation energy per residue nucleon, $\langle E^{*}/A \rangle$, extends to larger values for ^{107}Ag, as shown in Fig. 14. The maximum values correspond to $E^{*}/A \approx 13$ MeV per residue nucleon for the Ag target and $E^{*}/A \approx 9$ MeV/residue nucleon for ^{197}Au.

V. Conclusions

In summary, we have investigated the collision dynamics in GeV light-ion-induced reactions by

measuring LCPs and IMFs with a low-threshold 4π charged-particle detector array. Several experimental observable related to the projectile energy dissipation and excitation deposited in the target-like residue have been examined. These include multiplicity distributions for LCPs, IMFs and total charged particles, total observed participant charge and the total emitted energy and its transverse component. In addition, on the basis of the systematic of the fragment LCP and IMF spectra, we have separated the distributions into thermal and fast components.

In terms of deposition energy--most relevant to defining the thermal properties of the residues--it is argued that the most valid experimental signatures are found in the IMF and total-thermal-LCP multiplicities and the thermalized energy. Correlations of these observable with the average IMF multiplicity reinforce this conclusion. We also show that the total thermal energy distribution scales with that for total transverse energy; however, the total transverse energy is also sensitive to nonequilibrium events. The LCP and total-charged-particle multiplicities, as well as the total observed energy per event are shown to contain significant fast-cascade/nonequilibrium components. Thus, they relate more to the energy dissipated by the **projectile than to the excitation energy** deposited in the residue. The presence of significant nonequilibrium emission in these data **emphasizes** the importance of eliminating such events in any attempt to evaluate the residue excitation energy.

For all distributions, the maximum value of a given observable increases as a function of increasing projectile energy for each target and as a fraction of **projectile mass** for a fixed bombarding energy. The exception is the ^{3}He + ^{nat}Ag system, where the results show a saturation in deposition energy near 4 GeV. This is consistent with the observation of limiting fragmentation and constant charge distributions for light-ion-induced reactions in this energy region. From the thermal energy distributions and the associated fragment charge distributions, we estimate the most violent events produce deposition energies Up to $E^{*} \sim 950$ MeV for ^{nat}Ag and E“ -1600 MeV for ^{197}Au. These values correspond to maximum values of $E^{*}/A \sim 12$ MeV for the Ag-like residue and E^{*}/A -10 MeV for the Au-like residue--indicating that the total LCP vaporization regime should be accessible in GeV light-ion-induced reactions.

Finally, comparison of the experimental results with the intranuclear cascade code ISABEL shows good qualitative correspondence. In particular, the code predicts the observed saturation in deposition energy for the $^{3}He + ^{nat}Ag$ system near 4 GeV bombarding energy. In addition, the predicted relative cross section for excitation energies that exceed the multifragmentation threshold (-500 MeV) appear to be consistent with the cross section values determined in Ref. 23. Thus, the INC model appears to provide a reasonable basis for describing the collision dynamics in GeV light-ion reactions. However, a quantitative relationship between the experimental observable and transport code predictions of the deposition energy remains an important future objective.

We thank the technical staff of DAPNIA/CE Saclay, as well as J. Arvieux and the staff at LNS for their support in making these experiments possible; in particular, G. Milleret for his assistance with the beam tuning optics. Among the numerous individuals who contributed to the success of this project were Mine. F. Haroutel, Mine. A. Mansion, J. Faure, J. C. Lugol and his staff, W. Lozowski, J. P. Passerieux, C. Mazur, K. McDonald, T. Hamilton, C. Powell, J. Dorsett, A. Alexander, J. Poehlman and K. Komisarcik. We also thank Z. Fraenkel for providing the ISABEL code to us and W. Bauer and P. Danielewicz for fruitful discussions of the reaction dynamics. The authors acknowledge the primary financial support of the U.S. Department of Energy; additional support was provided by Indiana University, Commissariats à l'Energie Atomique (France), the U.S. National Science Foundation, the National Science and Energy Research Council (Canada), NATO, and KBN grant 0719/P3/93/04 (Poland).

References:

1. R. Wolfgang, E. W. Baker, A. A. Caretto, J. B. Cumming, G. Friedlander and J. Hudis, Phys. Rev. IQ 394 (1956).
2. J. Cugnon, D. Kinet and J. Vandermuelen, Nucl. Phys. A 379, 553 (1982): 462, 751 (1987).
3. Y. Yariv and Z. Fraenkel, Phys. Rev. C 24, 488 (1981); Phys. Rev. C 20, 2227 (1979).
4. K. Kwiatkowski, W. A. Friedman, L. W. Woo, V. E. Viola, E. C. Pollacco, C. Volant and S. J. Yennello, Phys. Rev. C 49, 1516 (1994).
5. G. Wang, K. Kwiatkowski, V. E. Viola, W. Bauer and P. Danielewicz, Indiana Report, INC-40007-106, 1995, accepted for publication in Phys. Rev. C.
6. A. Y. Abdul-Magd, W. A. Friedman and J. Hüfner, Phys. Rev. C 34, 113 (1986).
7. V. S. Barashenkov, A. S. Iljinov and V. D. Toneev, Sov. J. Nucl. Phys. 13, 422 (1971): Acta Phys. Polonica B 1, 219 (1973); E. S. Golubeva et al., Phys. At. Nucl. 57, 2084 (1994).
8. G. F. Bertsch, H. Kruse and S. Das Gupta, Phys. Rev. C 29, 673 (1984).
9. P. Danielewicz and G. F. Bertsch, Nucl. Phys. A 533, 712 (1991): P. Danielewicz, private communication.
10. W. Bauer, G. F. Bertsch, W. Cassing and U. Mosel, Phys. Rev. C 34, 2127 (1986); B. -A. Li, W. Bauer and G. F. Bertsch, Phys. Rev. C 44, 2095 (1991).
11. W. Bauer, G. F. Bertsch and H. Schulz, Phys. Rev. Lett. 69, 1888 (1992).
12. L. G. Moretto, K. Tso, N. Colonna and G. J. Wozniak, Phys. Rev. Lett. 69, 1884 (1992).
13. S. Pratt, Phys. Rev. A 42, 1447 (1990); S. Pratt et al., Phys. Lett. B 349, 251 (1995),
14. W. G. Lynch, Ann. Rev. Nucl. Sci. 37,493 (1987).
15. K. Nakai, Nucl. Phys. A 379, 553 (1982): A 462, 751 (1987).
16. A. 1. Warwick, H. H. Wieman, H. H. Gutbrod, M. R. Maier, J. Péter, H. Stelzer and F. Welk, Phys. Rev. C 27, 1083 (1983).
17. F. Saint Laurent, M. Conjeaud, R. Dayras, S. Harar, H. Oeschler and C. Volant, Nucl. Phys. A 422, 307 (1984).

18, M. Fatyga, K. Kwiatkowski, H. J. Karwowski, L. W. Woo and V. E. Viola, Phys. Rev. C 32, 1496 (1985); L. W. Woo, K. Kwiatkowski and V. E. Viola, Phys. Lett. B 132, 283 (1993).

19. G. Klotz-Engmann et al., Nucl. Phys. A 499, 392 (1989).

20. L. Pienkowski et al., Phys. Lett. B 336, 147 (1994).

21. K. B. Morley et al., Phys. Lett. B 355, 52 (1995).

22. K. Kwiatkowski et al., Phys. Rev. Lett. 74, 3756 (1995).

23. E. Renshaw Foxford et al., Phys. Rev. C (this issue).

24. K. Kwiatkowski et al., Nucl. Instr. Meth. A 360, 571 (1995).

25. W. Lozowski, Indiana University Cyclotron Facility.

26. J. P. Passerieux, CEN Saclay preprint (1993).

27. D. Powers, W. K. Chu, R. J. Robinson and A. S. Lodhi, Phys. Rev. A 6, 1425 (1972).

28. DONNA code, W. G. Meyer, unpublished.

29. W. A. Friedman, Phys. Rev. C 42, 667 (1990).

30. J. P. Bondorf, R. Donangelo, I. N. Mishustin, C. J. Pethick, H. Schulz and K. Sneppen, Nucl. Phys. A 443, 321 (1985).

31. D. H. E. Gross, Rep. Prog. Phys. 53, 605 (1990).

32. V. Lips et al., Phys. Rev. Lett. 72, 1604 (1994).

33. D. R. Bowman et al., Phys. Rev. Lett. 67, 1527 (1991).

34. W. Trautman, AIP Conf. Proc. 250, 409 (1991).

35. D. S. Bracken, Ph.D. Thesis, Indiana University, 1996.

36. G. Bertsch, in Nuclear Physics with Heavy Ions and Mesons, Vol. 1 (North Holland, ed. R. Balian, M. Rho and G. Ripka, 1978), p. 251.

37. J. Randrup and S. Koonin, Nucl. Phys. A 356, 223 (1981); J. A. Lopez and J. Randrup, Nucl. Phys. A&, 477 (1989).

38. J. Hubele et al., Zeit. Phys. A 340, 263 (1991).

39. G. F. Peaslee et al., Phys. Rev. C 49, R2271 (1994).

40. D. R. Bowman et al., Phys. Rev. C 46, 1834 (1992).

41. L. Phair et al., Phys. Lett. B 285, 10 (1992).

42. F. Saint-Laurent et al., Nucl. Phys. A 583, 481 (1995).

43. D. J. Morrissey, W. Loveland, M. de Saint Simon and G. T. Seaborg, Phys. Rev. C 21, 1783 (1980).

44. G. F. Bertsch, H. Kruse and S. Das Gupta, Phys. Rev. C 29, 673 (1984).

45. H. Kruse, B. V. Jacak, J. J. Molitoris, G. D. Westfall and H. Stocker, Phys. Rev. C 31, 1770 (1985).

46. J. Aichelin, Phys. Rep. 202, 233 (1991).

Table 1.

The number of valid trigger events (multiplicity ≥ 2) after data have been filtered through the gating conditions.

System	Total Events	Events with at least one IMF
1.8 GeV $^{3}He + ^{nat}Ag$	5,405,691	822,993
3.6 GeV $^{3}He + ^{nat}Ag$	6,301,388	1,606,407
4.8 GeV $^{3}He + ^{nat}Ag$	4,636,509	1,276,631
1.8 GeV $^{3}He + ^{197}Au$	1,178,124	267,543
4.8 GeV $^{3}He + ^{197}Au$	3,928,244	1,639,313

Figure Captions:

Fig. 1 Configuration for one arc of detector telescopes in forward hemisphere for Indiana Silicon Sphere [24]. Four annular segments containing eighteen such arcs fit together to cover one hemisphere from 14° to 86.5° in polar **angle. At the smallest** angles, each detector module is divided into two halves to increase **granularity. The x axis coincides** with the beam direction.

Fig. 2 Experimental layout at the Saturne II accelerator for **experiment E228. Detector** elements include the ISiS array, the recoil array, and the forward plastic wall (ARCOLE). Equipment related to the beam quality includes **two x-y position-sensitive** profilers, a 50 cm-long lead collimator, beam halo counters (active collimators) and a secondary emission monitor.

Fig. 3 Measured IMF multiplicity distributions for (top) the 1.8 and 4.8 GeV $^{3}He + ^{197}Au$ reactions and (bottom) 1.8, 3.6 and 4.8 GeV $^{3}He + ^{nat}Ag$ reactions. Error bars are statistical only. Distributions are not corrected for detector geometric efficiency.

Fig. 4 Measured LCP and total **charged-particle multiplicity distributions** for the 1.8 and 4.8 GeV $^{3}He + ^{197}Au$ reactions (top) and 1.8, 3.6 and 4-8 GeV $^{3}He + ^{nat}Ag$ reactions (bottom). Error bars are statistical only.

Fig. 5 Spectra of He, Li, and C fragments for M_{IMF} = 2 events at 14° - 22°. Data are from 4.8 GeV $^{3}He + ^{197}Au$ system< Solid lines are two-component moving-source fits to the Li and C spectra; dashed lines represent the corresponding slow component.

Fig. 6 Comparison of thermal (left) and fast (right) multiplicity distributions for the $^{3}He + ^{nat}Ag$ system, as described in text. Systems are defined on figure.

Fig. 7 Total emitted energy per event for $^{3}He + ^{197}Au$ system (left frame) and $^{3}He + ^{nat}Ag$ (right frame).

Fig. 8 Lower frames: Distributions of observed total thermalized energy per event for $^{3}He + ^{197}Au$ (left) and $^{3}He + ^{nat}Ag$ (right); upper frames: Correlation between total thermalized energy and transverse energy. Error bars indicate standard deviations of distribution widths ($\pm\sigma$) and are representative of data. Systems are defined on figure.

Fig. 9 Total observed charge for the 1.8 and 4.8 GeV $^{3}He + ^{197}Au$ reactions (left) and 1.8, 3.6 and 4.8 GeV $^{3}He + ^{nat}Ag$ reactions (right).

Fig. 10 The average number of observed IMFs $<N_{IMF}>$ as a function of LCP (left) and total charged-particle (right) multiplicity for $^{3}He + ^{197}Au$ system (top) and $^{3}He + ^{nat}Ag$ system (bottom).

Fig. 11 $<N_{IMF}>$ as a function of total observed charge (left) and total thermalized energy (right) for $^{3}He + ^{197}Au$ system (top) and $^{3}He + ^{nat}Ag$ system (right).

fig. 12 LCP distributions for IMF multiplicities M_{IMF} = 1 -7 in the 4.8 GeV $^{3}He + ^{197}Au$ reaction.

Fig. 13 Predictions of the ISABEL code (with fast rearrangement option) for average excitation energy as a function of bombarding energy for the $^{3}He + ^{107}Ag, ^{197}Au$ systems. Results are shown for three impact-parameter regimes, as indicated in the figure.

Fig. 14 Excitation energy per residue nucleon and average mass loss during the cascade (AA) as a function of excitation energy as predicted by the ISABEL code for the 4.8 GeV $^{3}He + ^{107}Ag$ (solid lines), ^{197}Au (dashed lines) reactions.

Fig. 15 Distribution of excitation energies for residues with E" > 50 MeV predicted by the ISABEL code for the 1.8 and 4.8 GeV $^{3}He + ^{197}Au$ reactions (bottom) and 1.8, 3.6 and 4.8 GeV $^{3}He + ^{107}Ag$ reactions (top). Calculations are averaged over 100 MeV bins. Symbols refer to projectile energy as follows: 1.8 GeV (circles); 3.6 GeV (diamonds) and 4.8 GeV (squares).

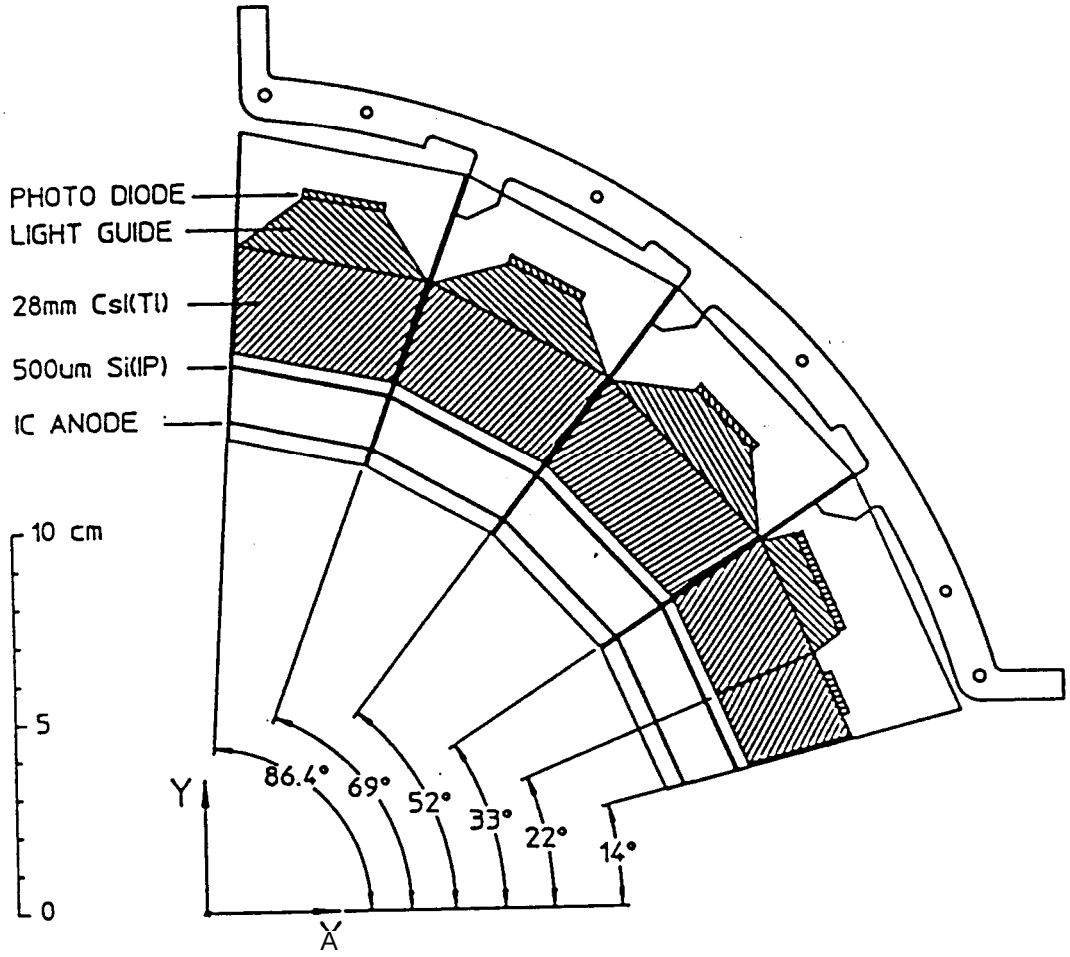
PHOTO DIODE
LIGHT GUIDE
28mm CsI(Tl)
500um Si(IP)
IC ANODE
10 cm
5
0
Y
X
86.4°
69°
52°
33°
22°
14°

Fig. 1

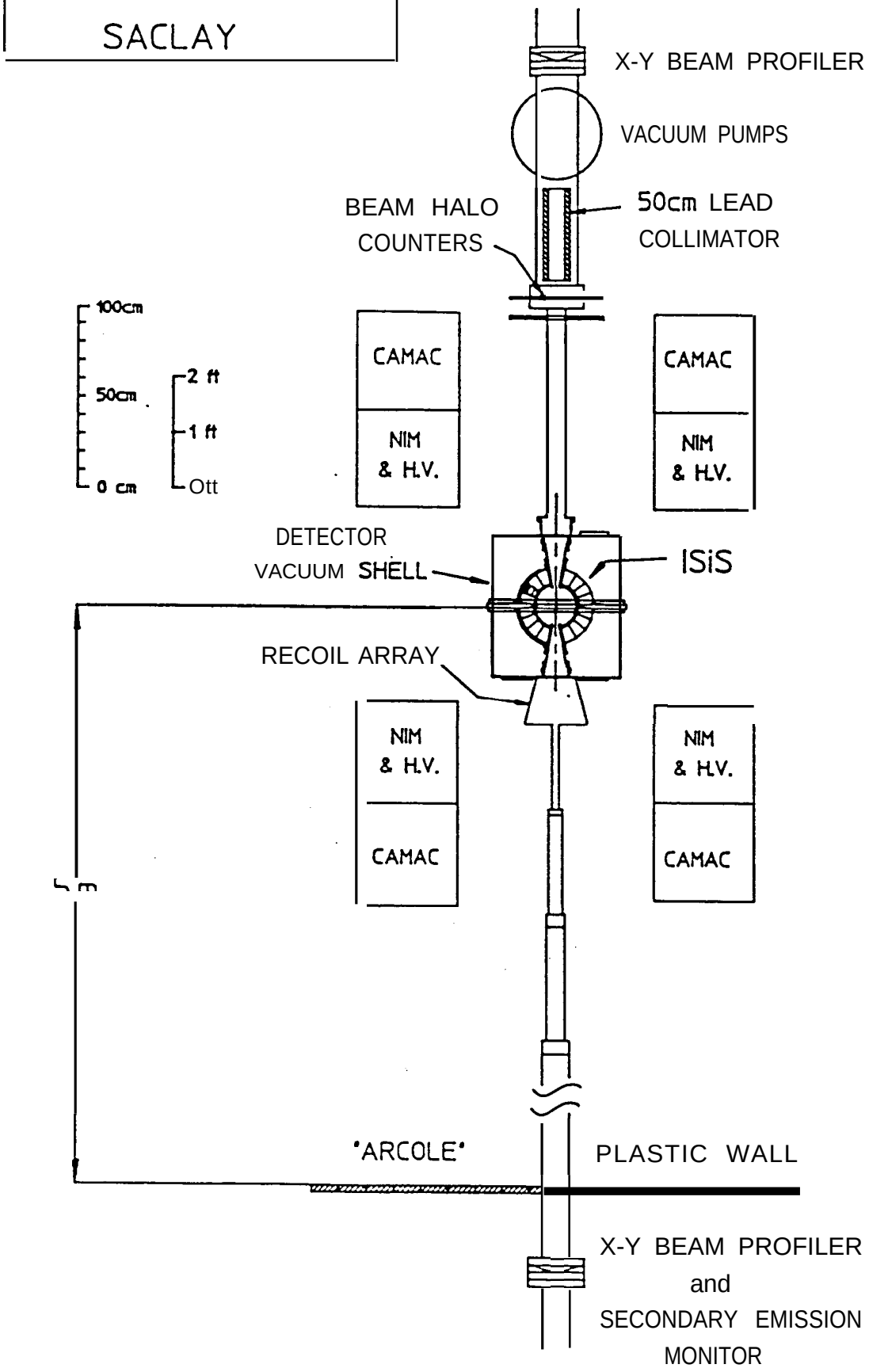
E228 AT SATURNE II
SACLAY
X-Y BEAM PROFILER
VACUUM PUMPS
BEAM HALO
COUNTERS
50cm LEAD
COLLIMATOR
100cm
50cm
0 cm
2 ft
1 ft
Ott
CAMAC
NIM
& H.V.
CAMAC
NIM
& H.V.
DETECTOR
VACUUM SHELL
ISiS
RECOIL ARRAY
NIM
& H.V.
CAMAC
NIM
& H.V.
CAMAC
5 m
'ARCOLE'
PLASTIC WALL
X-Y BEAM PROFILER
and
SECONDARY EMISSION
MONITOR

Fig. 2

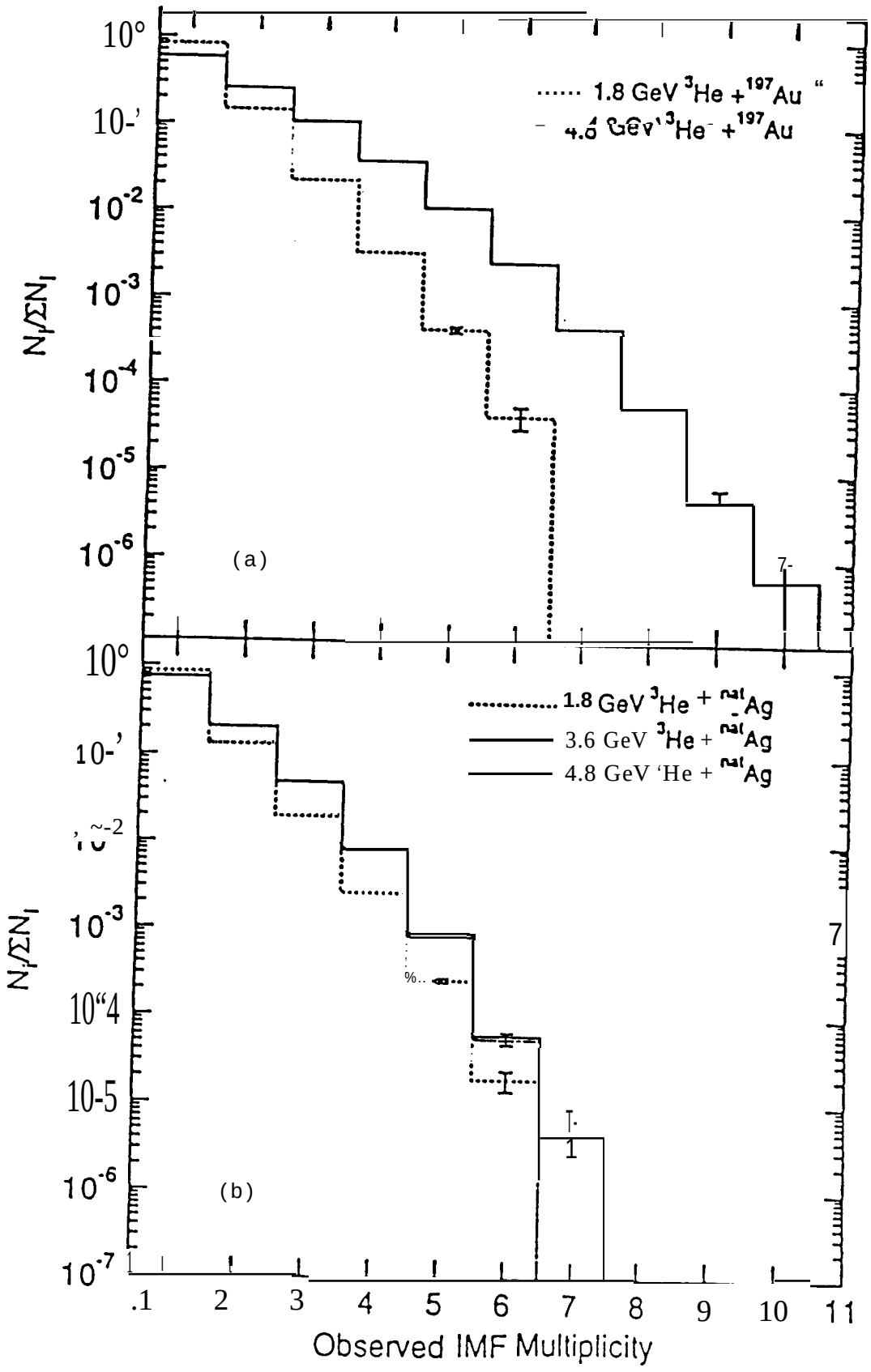
1.8 GeV ^{3}He + ^{197}Au
4.8 GeV ^{3}He + ^{197}Au
(a)
1.8 GeV ^{3}He + ^{nat}Ag
3.6 GeV ^{3}He + ^{nat}Ag
4.8 GeV ^{3}He + ^{nat}Ag
(b)
N/ΣN
Observed IMF Multiplicity

Fig. 3

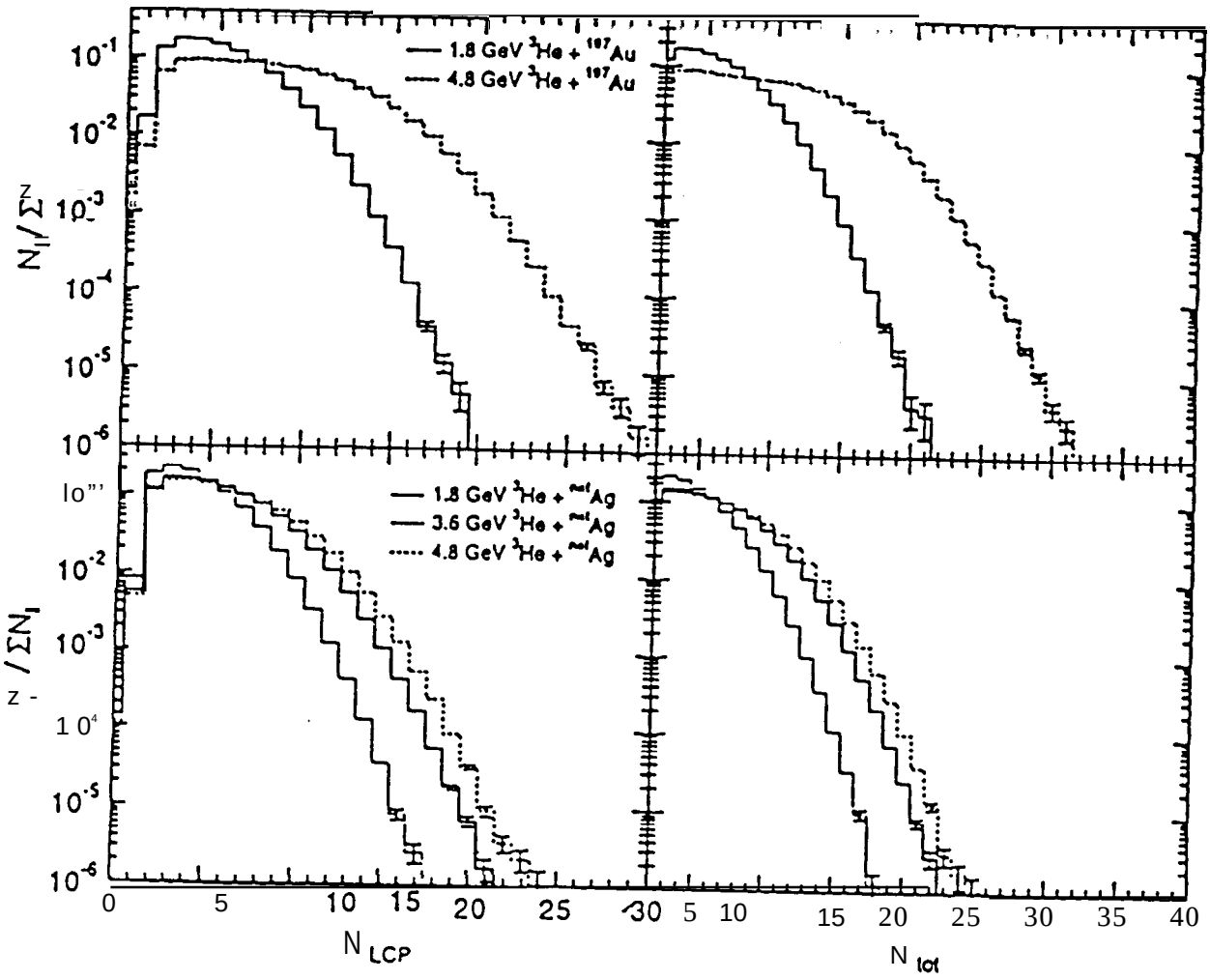
1.8 GeV 3He + 197Au
4.8 GeV 3He + 197Au
1.8 GeV 3He + natAg
3.6 GeV 3He + natAg
4.8 GeV 3He + natAg
N_i/ΣN_i
N_LCP
N_tot

Fig. 4

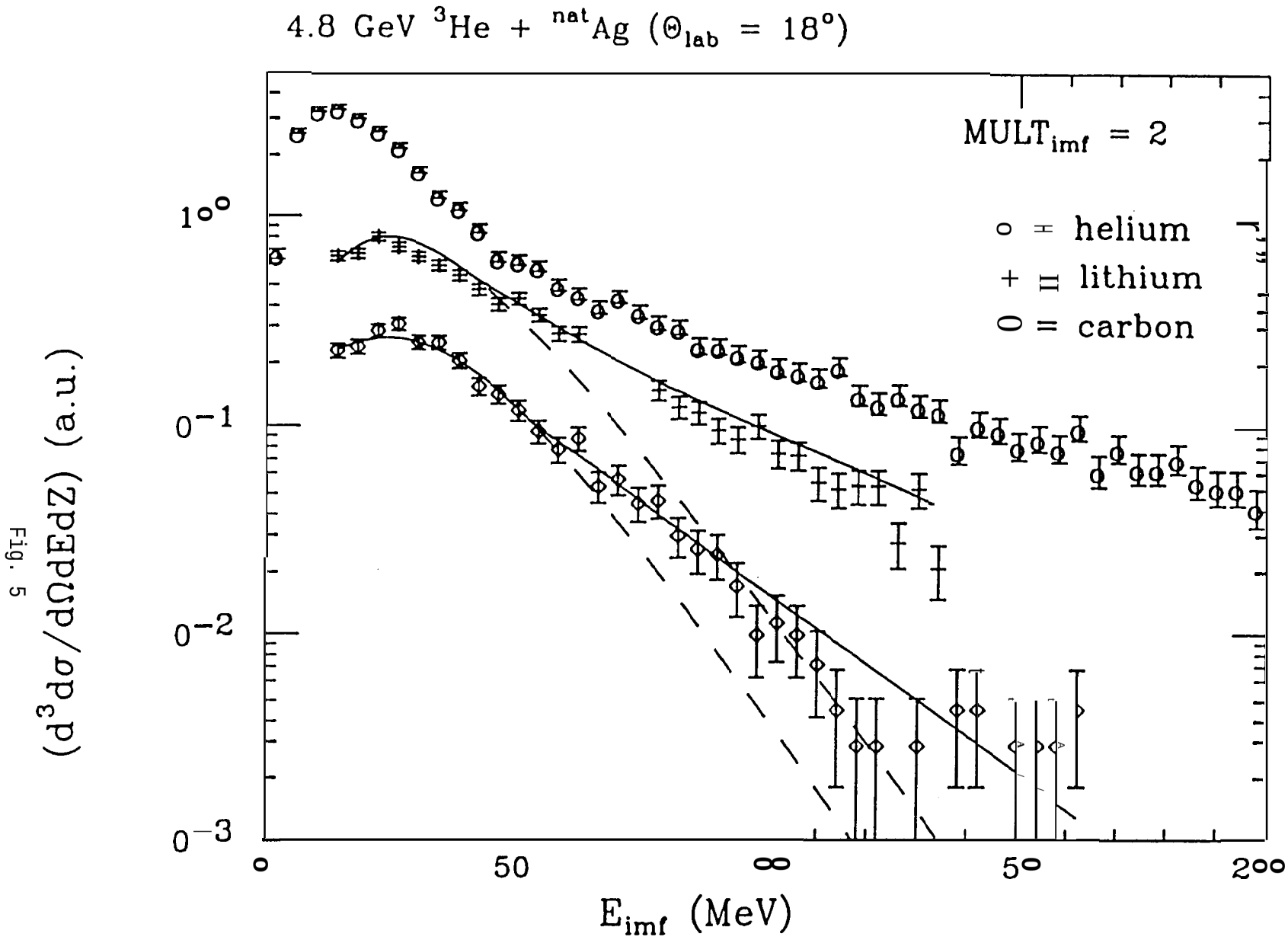
4.8 GeV ^{3}He + ^{nat}Ag (Θ_{lab} = 18°)
MULT$_{imf}$ = 2
o = helium
+ = lithium
□ = carbon
$(d^3d\sigma/d\Omega dEdZ)$ (a.u.)
10^0
10^{-1}
10^{-2}
10^{-3}
0
50
100
150
200
E_{imf} (MeV)

Fig. 5

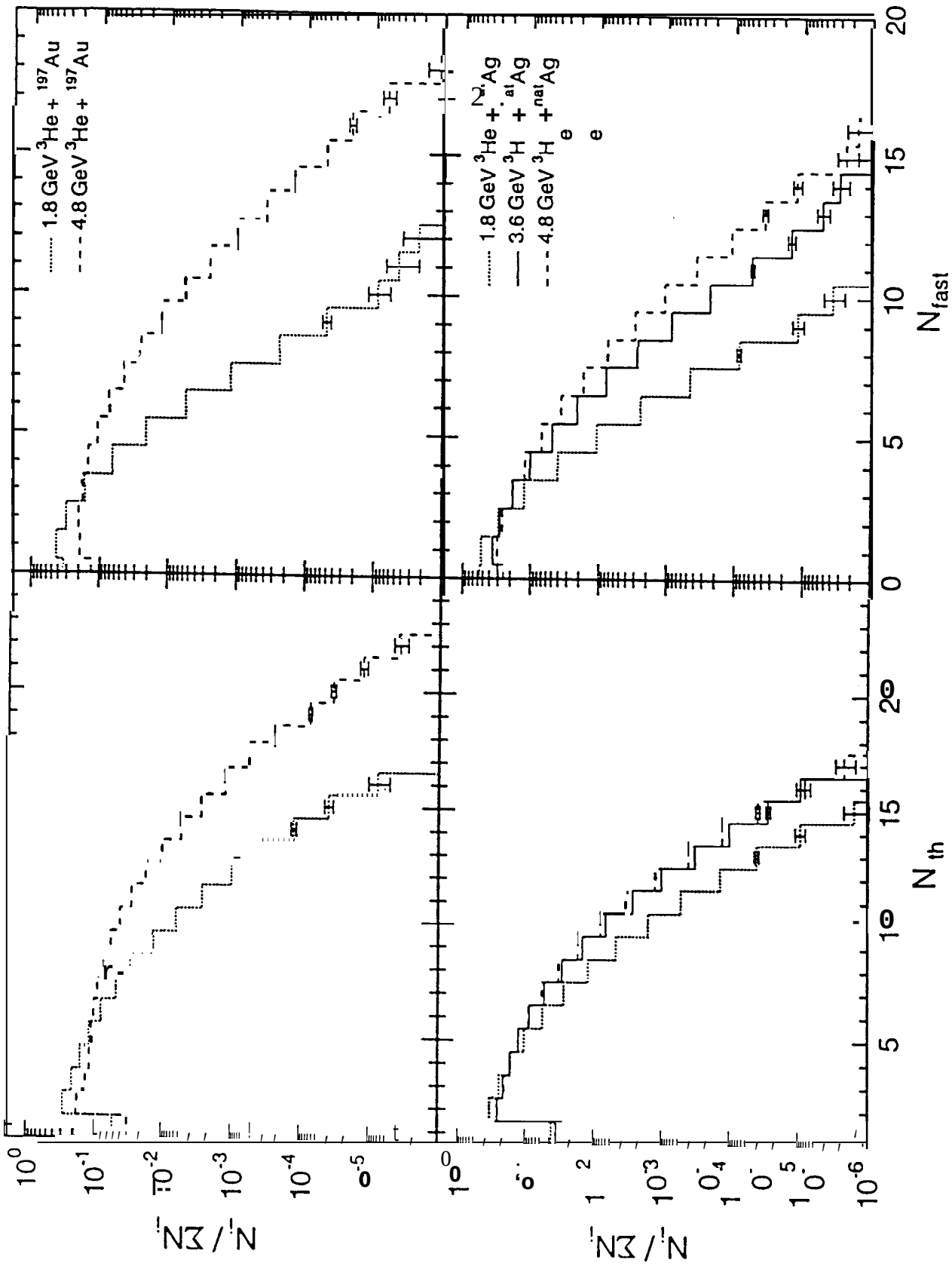
1.8 GeV ^{3}He + ^{197}Au
4.8 GeV ^{3}He + ^{197}Au
1.8 GeV ^{3}He + ^{nat}Ag
3.6 GeV ^{3}H + ^{nat}Ag
4.8 GeV ^{3}H + ^{nat}Ag
N_{fast}
N_{th}
$N_i / \Sigma N_i$
$N_i / \Sigma N_i$

Fig. 6

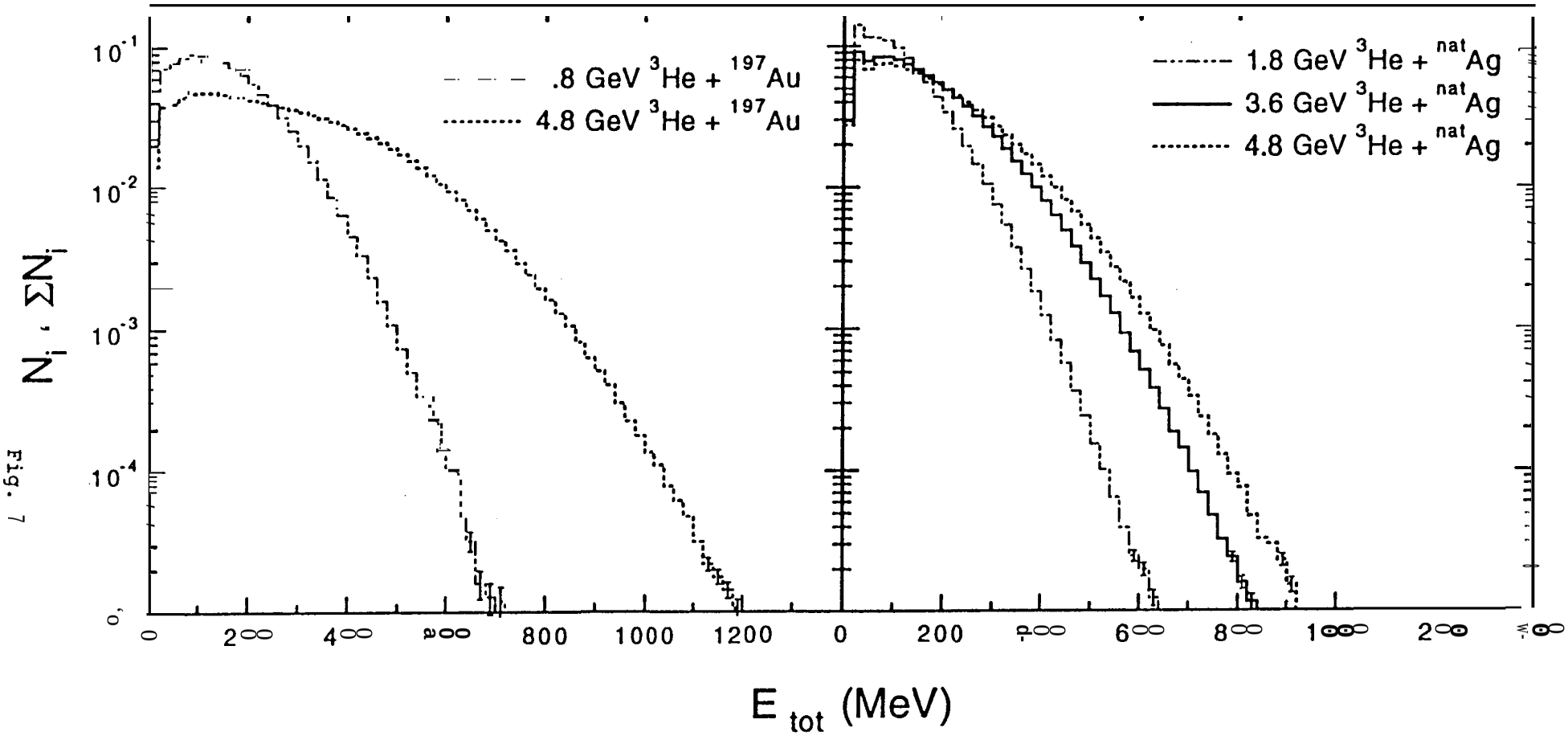
.8 GeV ^{3}He + ^{197}Au
4.8 GeV ^{3}He + ^{197}Au
1.8 GeV ^{3}He + ^{nat}Ag
3.6 GeV ^{3}He + ^{nat}Ag
4.8 GeV ^{3}He + ^{nat}Ag
N_i , ΣN_i
E_{tot} (MeV)

Fig. 7

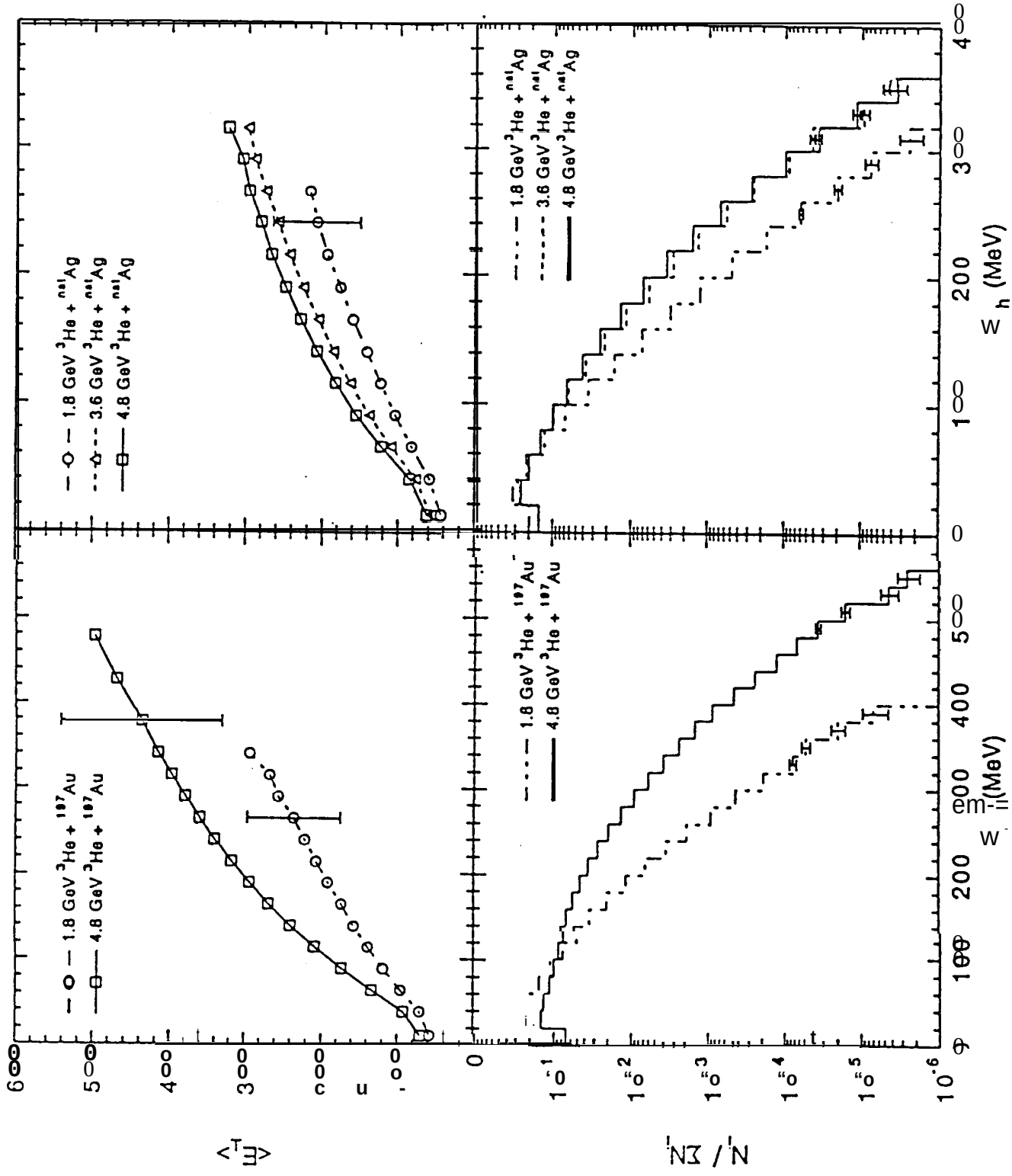
1.8 GeV ^{3}He + ^{nat}Ag
3.6 GeV ^{3}He + ^{nat}Ag
4.8 GeV ^{3}He + ^{nat}Ag
1.8 GeV ^{3}He + ^{197}Au
4.8 GeV ^{3}He + ^{197}Au
$\langle E_T \rangle$
$N_i / \Sigma N_i$
W_h (MeV)
W_{em} (MeV)

Fig. 8

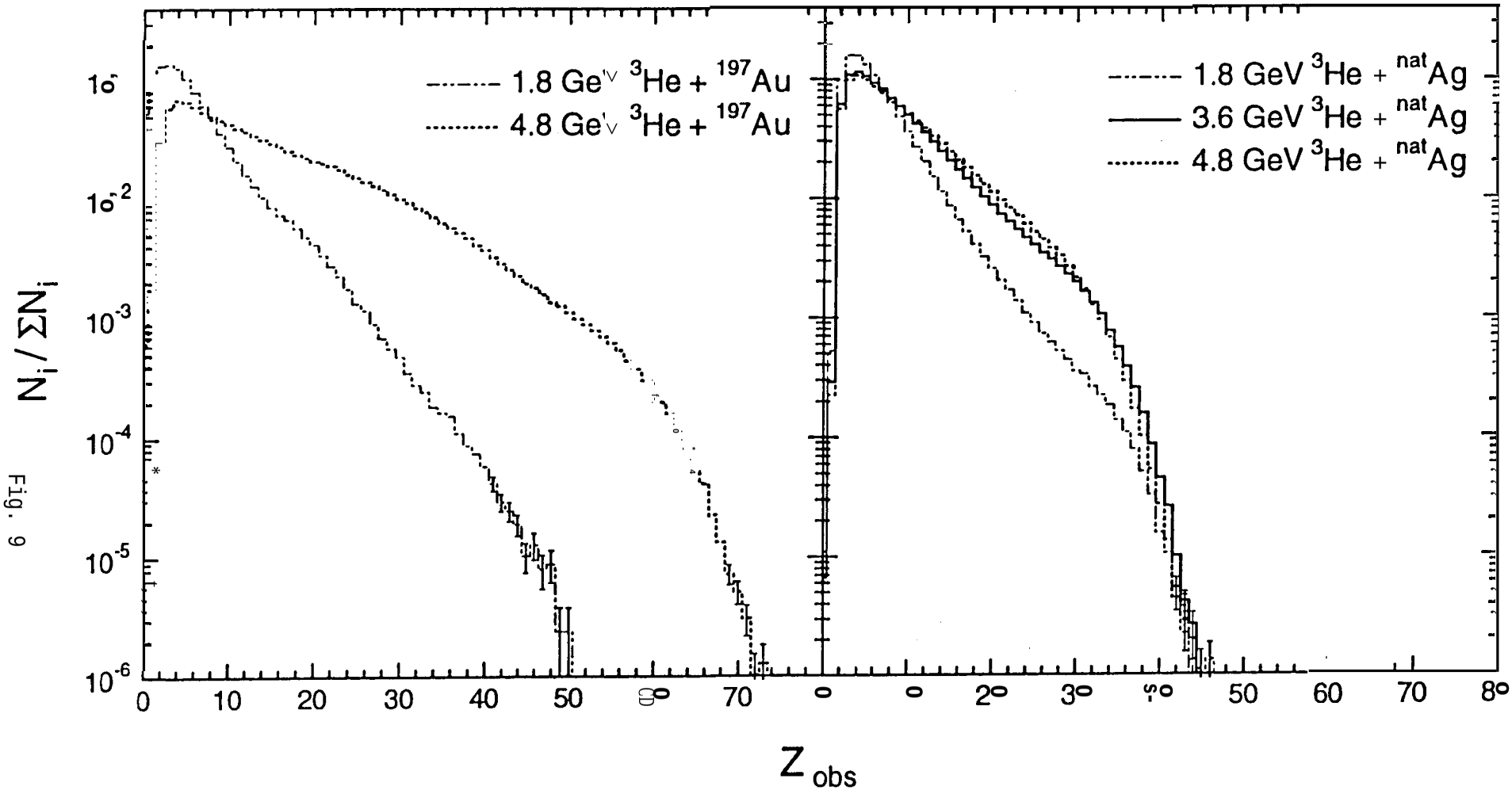
1.8 GeV ^{3}He + ^{197}Au
4.8 GeV ^{3}He + ^{197}Au
1.8 GeV ^{3}He + ^{nat}Ag
3.6 GeV ^{3}He + ^{nat}Ag
4.8 GeV ^{3}He + ^{nat}Ag
$N_i / \Sigma N_i$
Z_{obs}

Fig. 9

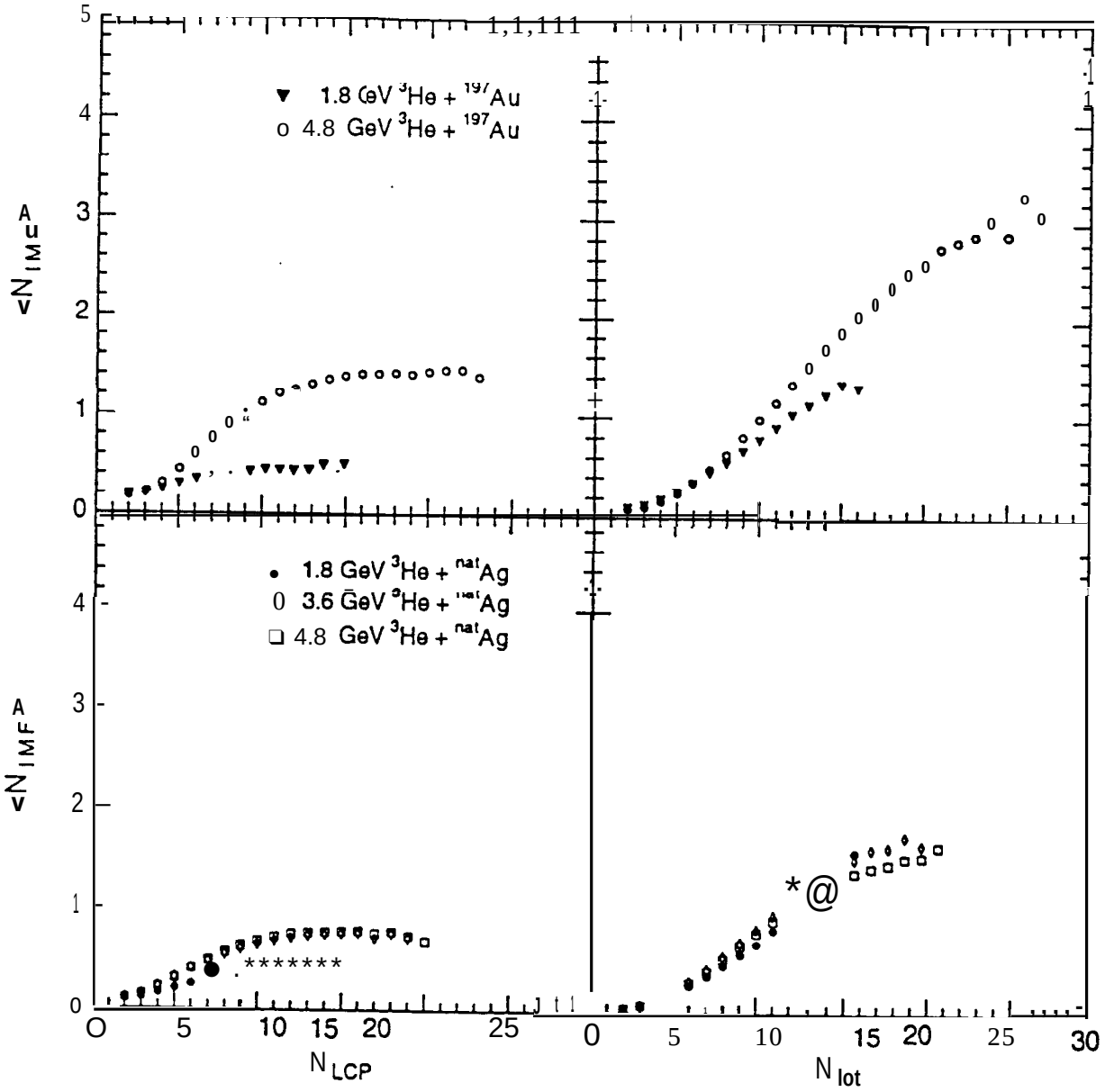
▼ 1.8 GeV ^{3}He + ^{197}Au
o 4.8 GeV ^{3}He + ^{197}Au
• 1.8 GeV ^{3}He + ^{nat}Ag
0 3.6 GeV ^{3}He + ^{nat}Ag
❑ 4.8 GeV ^{3}He + ^{nat}Ag
νN_{IMU}^{A}
νN_{IMF}^{A}
N_{LCP}
N_{tot}

Fig. 10

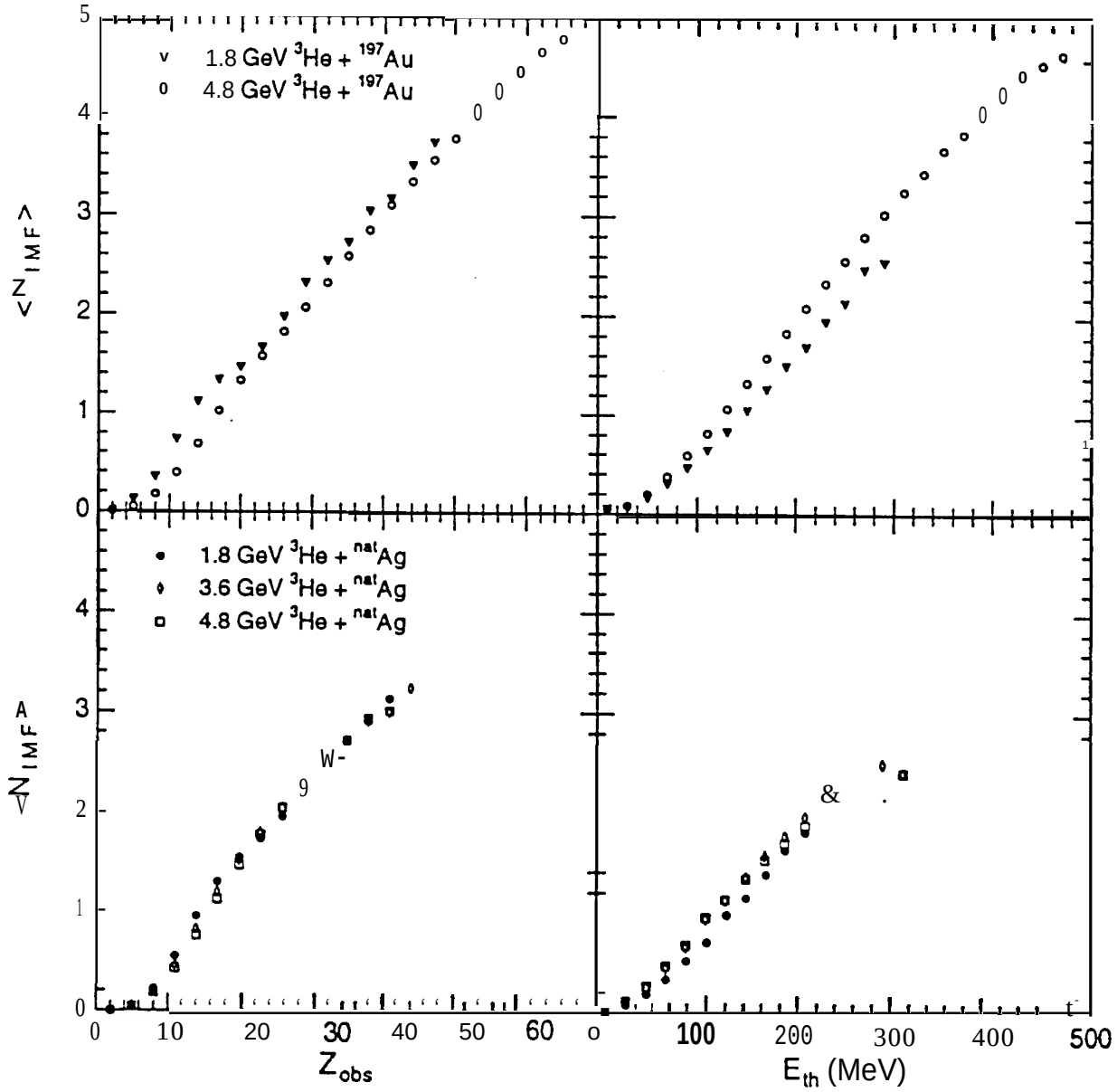
1.8 GeV 3He + 197Au
4.8 GeV 3He + 197Au
1.8 GeV 3He + natAg
3.6 GeV 3He + natAg
4.8 GeV 3He + natAg
<N_IMF>
N_IMF
Z_obs
E_th (MeV)

Fig. 11

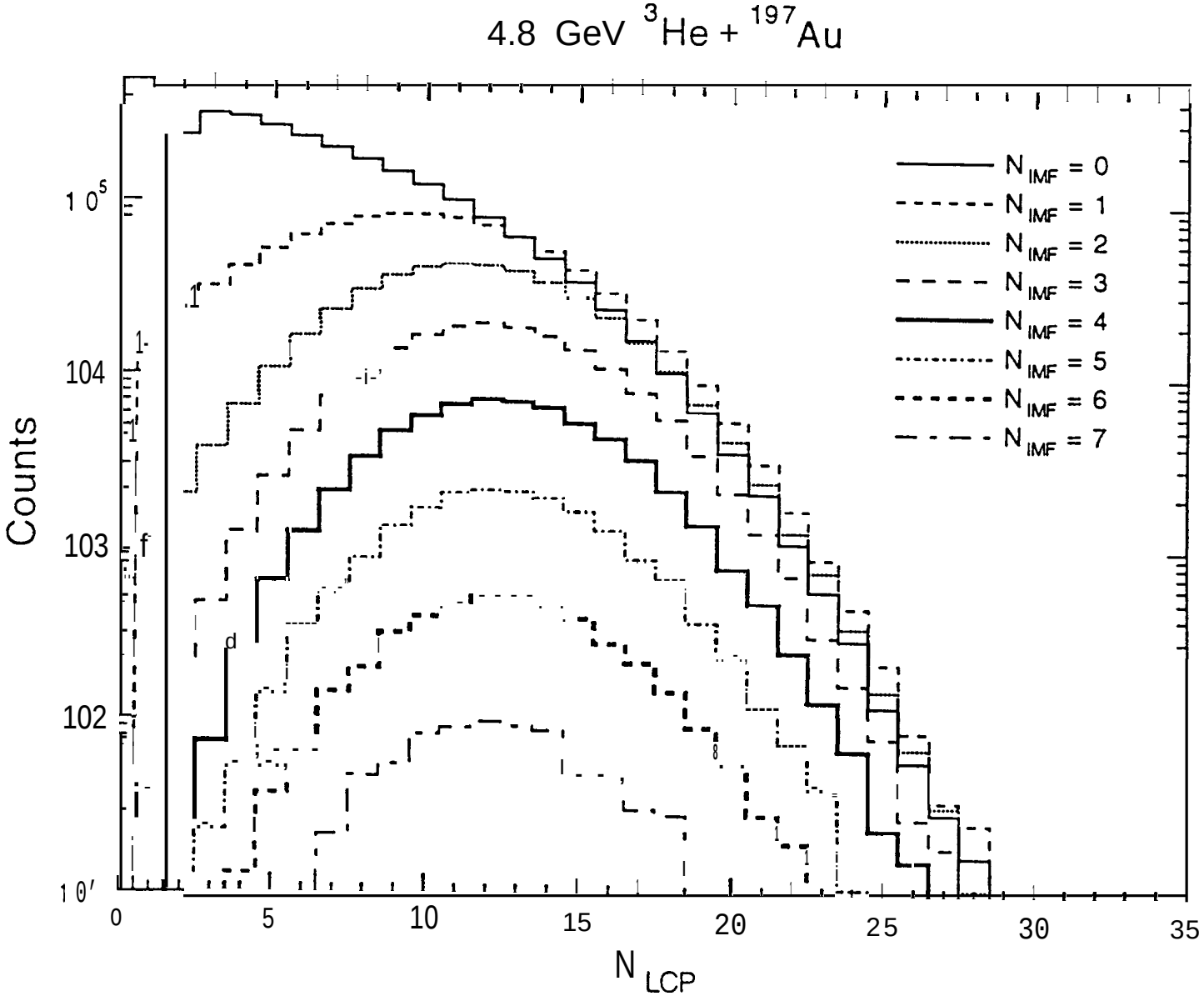
4.8 GeV ^{3}He + ^{197}Au
Counts
N_{LCP}
N_{IMF} = 0
N_{IMF} = 1
N_{IMF} = 2
N_{IMF} = 3
N_{IMF} = 4
N_{IMF} = 5
N_{IMF} = 6
N_{IMF} = 7

Fig. 12

Fig. 14

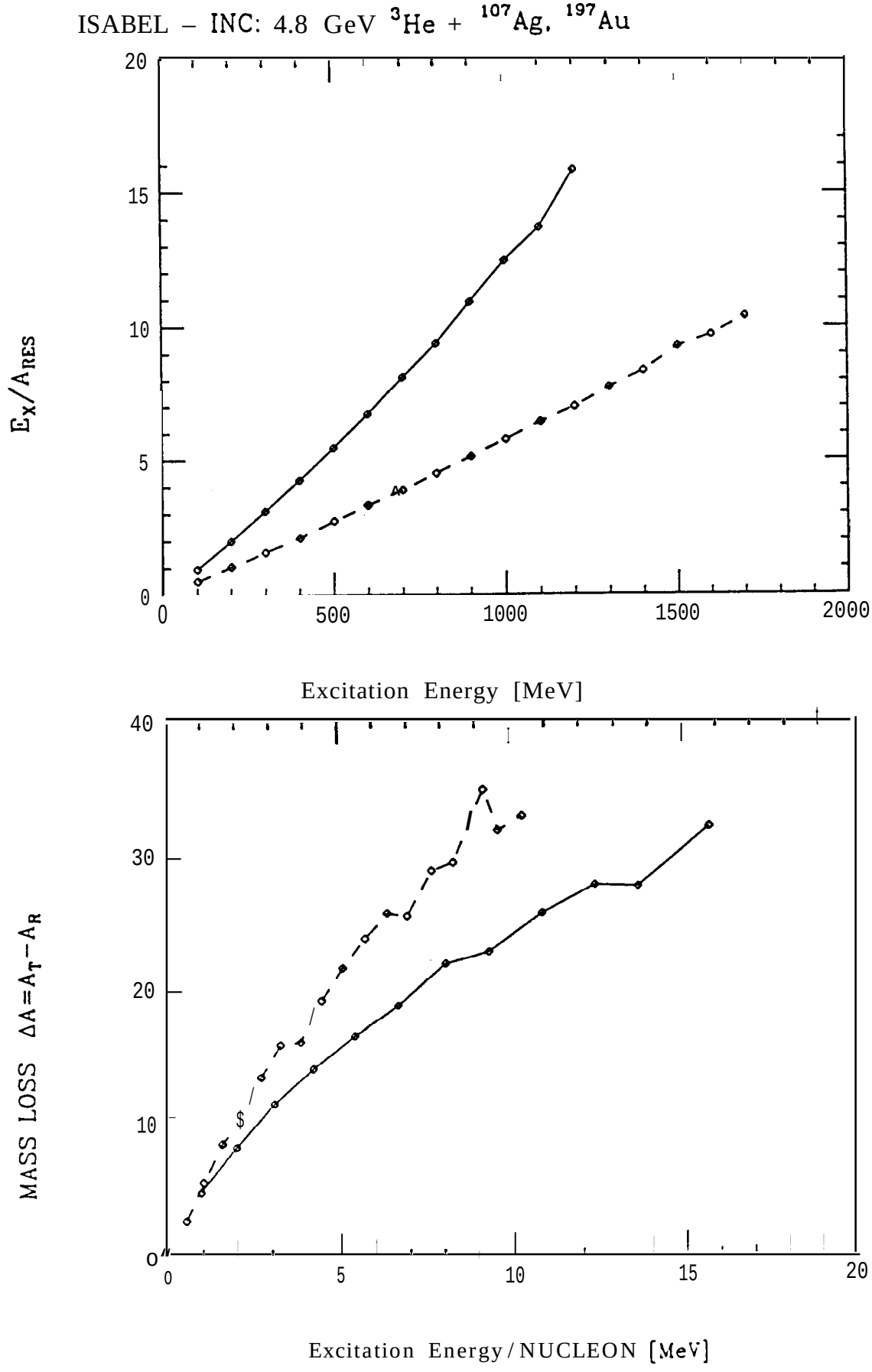
ISABEL – INC: 4.8 GeV ^{3}He + ^{107}Ag, ^{197}Au
E_X/A_{RES}
Excitation Energy [MeV]
MASS LOSS $\Delta A = A_T - A_R$
Excitation Energy / NUCLEON [MeV]

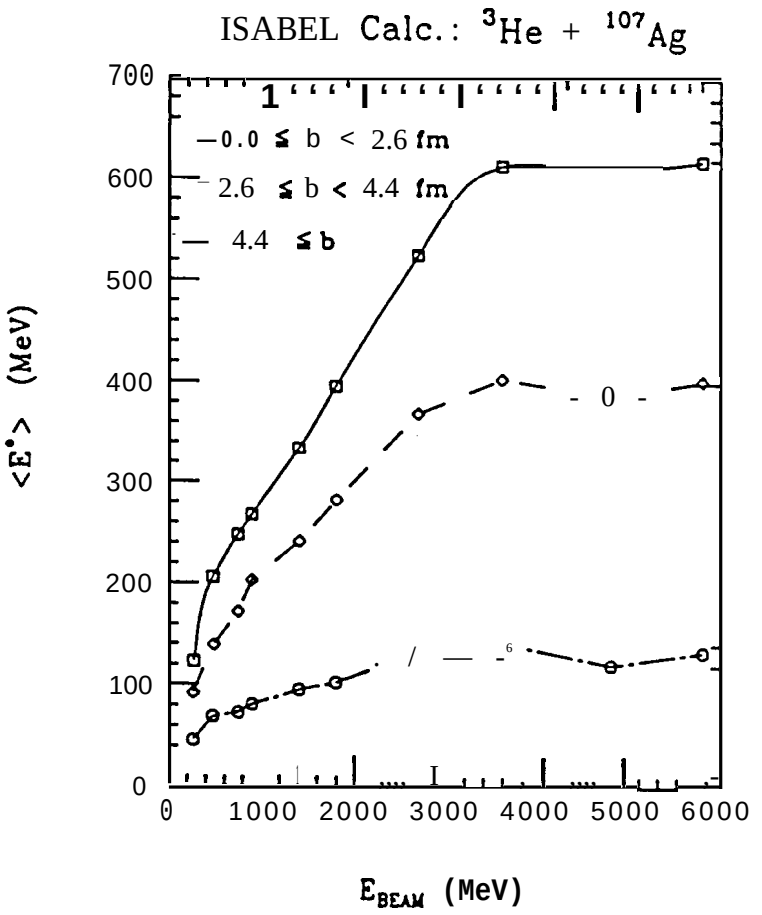
ISABEL Calc.: $^{3}He + ^{107}Ag$
0.0 ≤ b < 2.6 fm
2.6 ≤ b < 4.4 fm
4.4 ≤ b
<E*> (MeV)
E_{BEAM} (MeV)
0
100
200
300
400
500
600
700
0
1000
2000
3000
4000
5000
6000

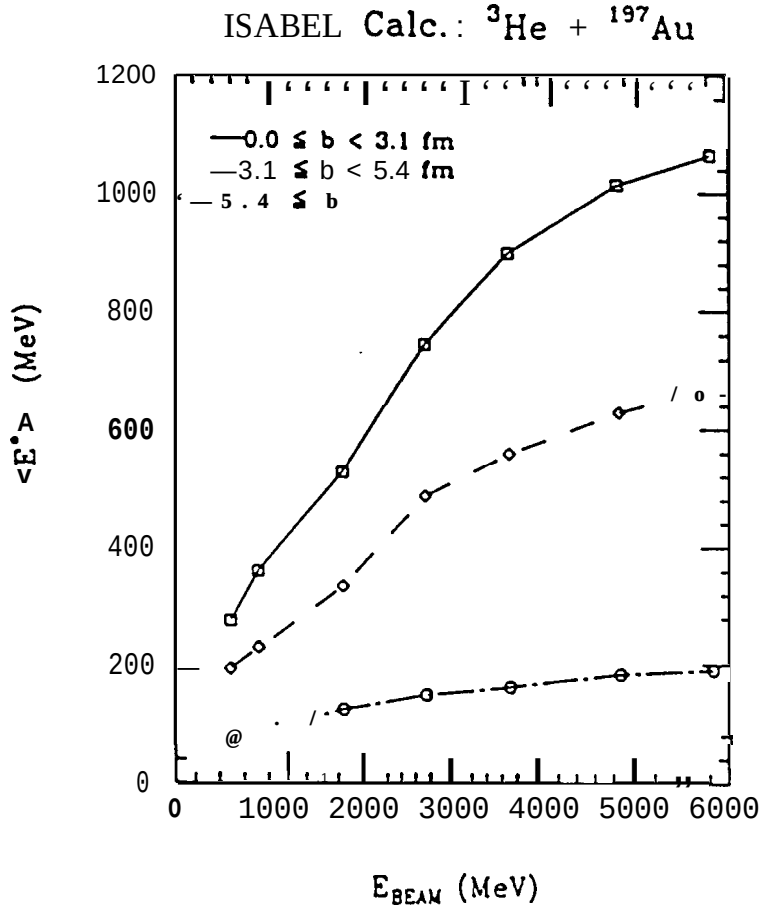
ISABEL Calc.: $^{3}He + ^{197}Au$
0.0 ≤ b < 3.1 fm
3.1 ≤ b < 5.4 fm
5.4 ≤ b
<E*A (MeV)
E_{BEAM} (MeV)
0
200
400
600
800
1000
1200
0
1000
2000
3000
4000
5000
6000

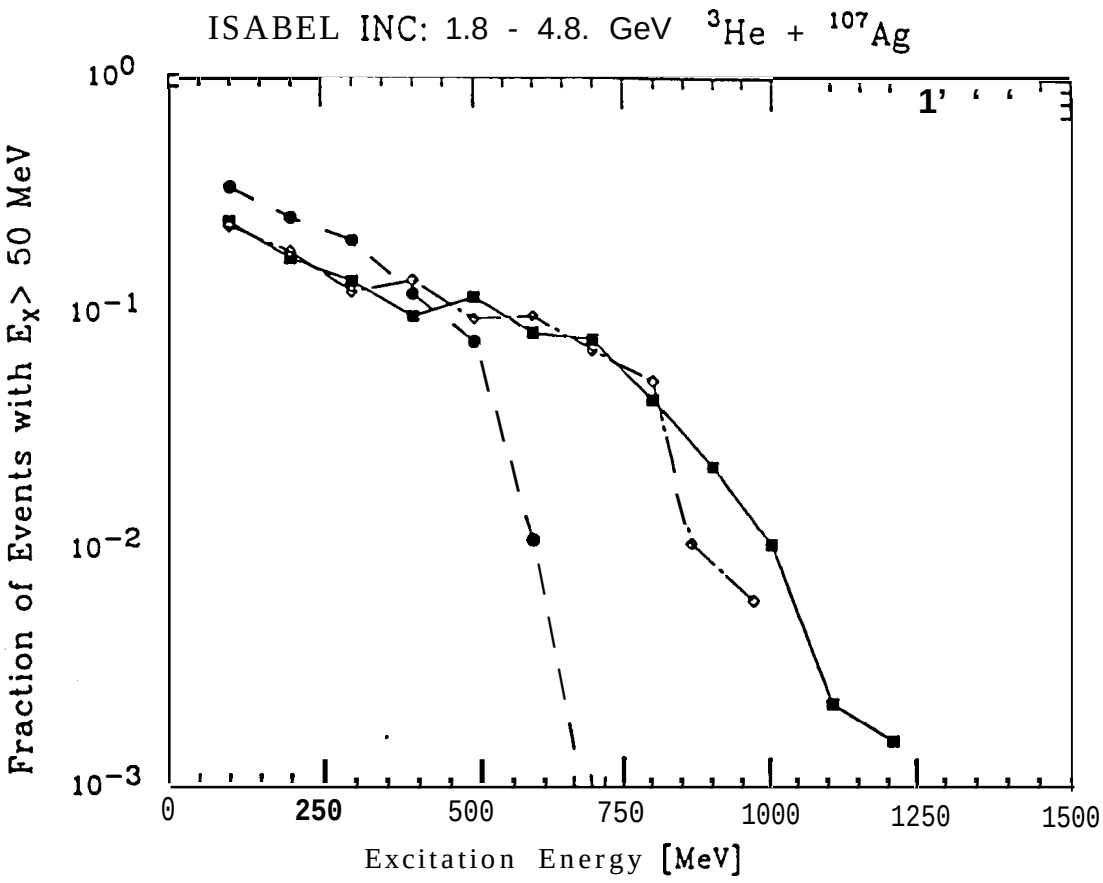
ISABEL INC: 1.8 - 4.8. GeV ^{3}He + ^{107}Ag
Fraction of Events with E_x> 50 MeV
10^{0}
10^{-1}
10^{-2}
10^{-3}
0
250
500
750
1000
1250
1500
Excitation Energy [MeV]

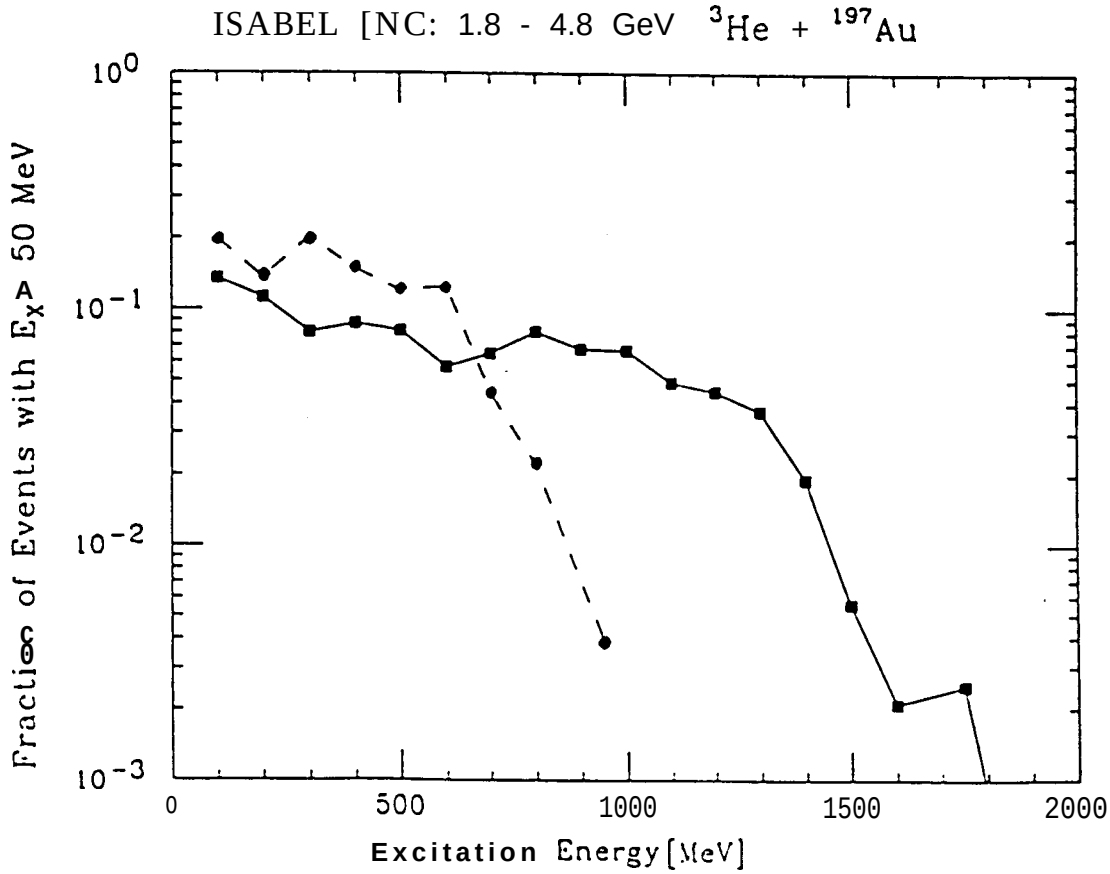
ISABEL [NC: 1.8 - 4.8 GeV ^{3}He + ^{197}Au
Fraction of Events with E_x 50 MeV
10^{0}
10^{-1}
10^{-2}
10^{-3}
0
500
1000
1500
2000
Excitation Energy [MeV]